Optically Pumped Perovskite DFB Lasers

Cheng Chang

A dissertation

submitted in partial fulfillment of the

requirements for the degree of

Doctor of Philosophy

University of Washington

2023

Reading Committee:

Lih Y. Lin, Chair
Arka Majumdar
Sajjad Moazeni

Program Authorized to Offer Degree:

Electrical and Computer Engineering

University of Washington

Abstract

Optically Pumped Perovskite DFB Lasers

Cheng Chang

Chair of the Supervisory Committee:
Lih Y. Lin
Department of Electrical and Computer Engineering

This dissertation focuses on metal halide perovskite lasers, which have garnered significant attention for their exceptional optoelectronic properties. The research presented in this dissertation adopts a chronological and in-depth approach to delve into various aspects of perovskite lasers.

The dissertation commences with an introduction to perovskites, followed by a brief review of perovskite lasers. Subsequently, it provides a comprehensive overview of perovskite material properties and carrier dynamics, fundamental to the understanding of perovskite applications. The synthesis of perovskite materials and the development of light-emitting devices are also explored.

Moving forward, the dissertation delves into research on perovskite lasers, emphasizing the design, fabrication, and optimization of 1st-order distributed feedback (DFB) lasers using specific perovskite compositions. The results showcase low lasing thresholds, while also

discussing techniques to further reduce thresholds and enhance device stability. These methods involve improved cavity design, material engineering, and thin film morphology engineering, collectively contributing to threshold reduction and overall performance enhancement. The research sheds light on the working dynamics of perovskite lasers and explores strategies to elevate their capabilities.

The dissertation also explores perovskite patterning techniques that integrate perovskites with nano-fabrication methods. Patterning techniques are crucial in sculpting MHPs into the desired on-chip components, enabling their seamless integration and unlocking their full potential in optoelectronics. These techniques enable the creation of complex perovskite photonic devices, including color converters, micro-LEDs, patterned LEDs, and potentially electrically pumped lasers.

Finally, the conclusion offers a comprehensive exploration of perovskite light-emitting applications, with a particular focus on lasers. The research presented in this dissertation significantly contributes to the understanding and advancement of perovskite-based optoelectronic devices, paving the way for their future applications in display and laser technologies.

TABLE OF CONTENTS

LIST OF FIGURES

LIST OF TABLES

ACKNOWLEDGEMENTS

I am deeply grateful for the enriching experience I have had during my five-year journey at the University of Washington for my Ph.D. studies. The support and contributions of numerous individuals have played a crucial role in shaping my academic and personal growth.

First and foremost, I express my heartfelt gratitude to Professor Lin for providing me with the opportunity to pursue my Ph.D. degree and for being my steadfast supervisor throughout this journey. I vividly recall the immense joy, excitement, and gratitude I felt when I received her offer. Over the past five years, Professor Lin has consistently guided, supported, enlightened, and encouraged me, and I owe much of my progress and achievements to her unwavering mentorship. I am particularly grateful for her genuine concern for my career development.

I extend my sincere thanks to our past and present group members, as well as my friends from other research groups: Chen Zou, Mark Odendahl, Yangwei Shi, Congyang Zhang, Lin Wang, Rose Johnson, Matthew Yerich, Changming Wu, Ruoming Peng, Bingzhao Li, Roger Fang, Seokhyeong Lee, Rui Chen, Di Sun, Zheyi Han, Yueyang Chen, Jiajiu Zheng, and Yifei Song. Their guidance, assistance, and companionship during my Ph.D. studies have been invaluable. We shared unforgettable experiences while working and living together, and these memories will remain among the most cherished moments of my life.

I would also like to express my gratitude to my collaborators for their support in my research endeavors. I sincerely appreciate the kindness of Professor Majumdar and Professor Li for allowing me to utilize their laboratories. The nano-photonics classes taught by these professors provided me with fantastic insights and ideas in the field. Additionally, the students from their groups generously assisted me with experiments and nano-fabrications. I am also thankful to Professor Moazeni for teaching me EE 538B photonic circuits, which greatly enhanced my understanding of system-scale photonic devices. I am grateful to Professor Zhang for joining my committee as GSR and providing valuable feedback during my general exam.

Lastly, I extend my thanks to the University of Washington for providing excellent research facilities. A significant portion of my work was carried out at the Molecular Analysis Facility (MAF), Washington Nanofabrication Facility (WNF), Photonic Research Center (PRC), and Research Training Testbed (RTT). These state-of-the-art facilities played a vital role in the success of my research endeavors.

Chapter 1. Introduction

1.1 Motivation for perovskite lasers

Metal halide perovskites (MPHs) are emerging semiconductor materials in the field of optoelectronics for the past decade. Owning to MPHs' intriguing optoelectronic properties, a dozen of devices based on perovskites have been brought up, such as solar cells, photodetectors, light emitting diodes, color converters and lasers. The bright future of high-performance, low-cost next-generation optoelectronic devices is being drawn by the quick advances and big leaps in perovskite studies.

Compared with other semiconductors, perovskites have high optical absorption, high carrier mobility, high defect tolerances, high photoluminescence quantum yield, narrow emission linewidth, long diffusion length, ambipolar charge transport, flexible turnability and low fabrication cost.[1-4] With these eminent optoelectronic properties, perovskites have been incorporated into various applications. Recently, the efficiency for perovskite solar cells and LEDs has reached 25.8%[5] and >28%[6,7] respectively.

Over the past decades, researchers have pursued the realization of perovskite lasers, envisioning them as the ultimate goal for perovskite materials. The unique blend of characteristics derived from both inorganic and organic semiconductors in perovskites positions them as promising candidates for the development of next-generation, cost-effective on-chip lasers (shown in Table 1). The striking advantages of perovskites are their relatively high mobility and gain coefficient, surpassing those of traditional organic materials and colloidal quantum dots (QDs). This enhanced performance in terms of carrier mobility and gain makes perovskite lasers highly attractive for various laser applications. Additionally, perovskites offer a notable edge in terms of fabrication cost when compared to conventional inorganic materials.

Their significantly lower cost of production opens up avenues for large-scale manufacturing, potentially revolutionizing laser technology with cost-effective solutions. Moreover, perovskites exhibit a tunable bandgap, a feature that proves invaluable in addressing the "green gap" challenge encountered in II-VI/III-V semiconductor lasers. This tunability allows researchers to tailor the emission wavelength to specific requirements, expanding the potential applications of perovskite lasers.

Materials	Emission spectrum (nm)	Mobility ($cm^{-2}V^{-1}s^{-1}$)	Gain coefficient (cm^{-1})
Inorganic	370-1500	100-1000	10-10000
Perovskites	400-1000	0.1-1000	10-1000
Organics	400-750	0.001-10	1-1000
Colloidal QDs	400-3600	0.001-0.01	10-100

Table 1 Comparison between perovskites and other gain mediums.

The very first study on perovskite lasing was reported in 1998 by Kondo, etc.[8] Then in 2004, their group demonstrated ASE from perovskite thin film, which paved the way for perovskite lasing devices.[9] The major breakthrough of perovskite lasers was brought in 2014. In that year, the low optical gain in $MAPbX_3$,[10] the first WGM perovskite laser[11], and the first room-temperature perovskite LED[12] with an EQE of 0.76% were reported. A promising future for perovskite laser diode was unveiled. Quickly after that, a series of optically pumped perovskite lasers have already been demonstrated, several types of perovskite lasers including Fabry-Pérot (FP) resonators,[13,14] photonic crystal lasers,[15,16] random lasers,[17] vertical-cavity surface-emitting lasers[18,19] (VCSEL) and DFB lasers[20] have been demonstrated. The pulsed lasing threshold has been pushed to as low as 220 nJ/cm^{-2},[21] and room-temperature CW lasing with a threshold of 5.7 W/ cm^{-2} has been achieved.[22]

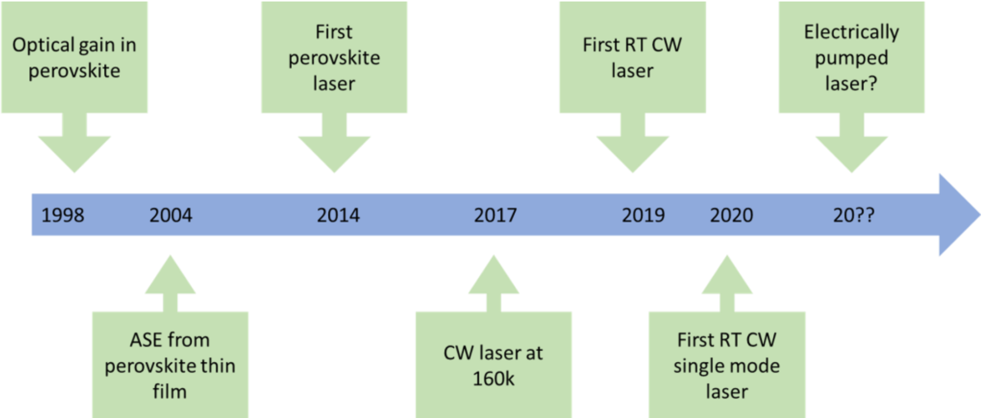

Figure 1 The development roadmap of perovskite lasers.

Among all the different laser designs, the most challenging and critical aspect is the resonant cavity for perovskite lasers due to the limited fabrication compatibility of perovskites. As a result, only a few options are available for creating resonant cavities in perovskite lasers. The first common option is to use the intrinsic cavity from perovskite single crystals, such as whispering gallery mode (WGM) cavities and nanowires (Figure 2 (a) & (d)). During the crystallization process, high-quality facets are formed at the perovskite crystal boundaries, serving as the reflection mirrors for the resonant cavity. However, these devices have limitations in controlling the cavity position and size, which can impact their performance. The second option involves using external cavities, such as distributed Bragg reflector (DBR), photonic crystal, and distributed feedback (DFB) cavities pre-fabricated on substrates (Figure 2 (b), (c)& (e)). Other techniques, like direct laser etching (Figure 2 (f)) or nanoimprints, have also been explored to directly pattern perovskites. However, to achieve improved perovskite quality, additional refinements and optimization steps are necessary.

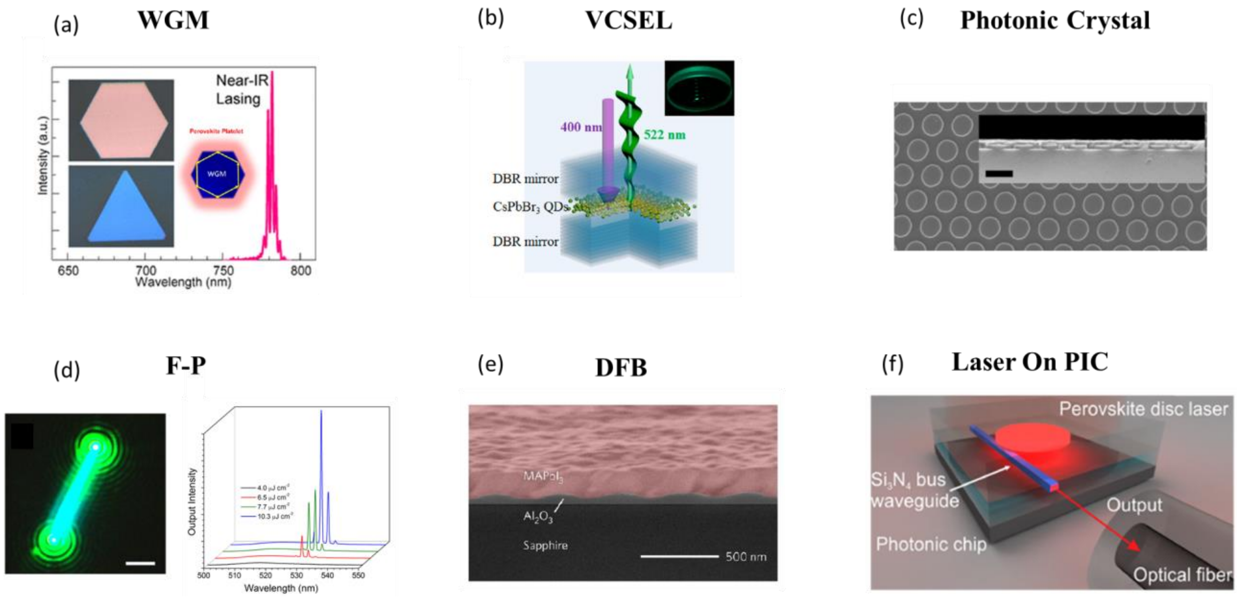

Figure 2 Perovskite lasers. (a) WGM laser from perovskite crystals.[11] (b)VCSEL laser with perovskite quantum dots.[19] The cavity is formed by two external DBR mirrors. (c) Photonic crystal laser.[16] (d) F-P cavity laser from perovskite nanowire.[14] (e) DFB laser.[20] (f) Pervskite disc laser by direct etching. [23]

While perovskites hold great promise as the next-generation material for optoelectronic devices, there is still a long way to go before they are commercially available for use in integrated circuits. The ultimate goal, electrically pumped perovskite lasers, has yet to be achieved. Perovskite devices suffer from poor stability, as they are susceptible to moisture, oxygen, UV light, and high heat. Additionally, ion migration leads to irreversible degradation under high electrical fields, which are common working conditions for electrically pumped lasers. Furthermore, perovskites dissolve in most polar solvents, including water and lithographic developers, which makes them incompatible with widely-used photolithographic processes necessary for nano-scale device fabrications. All of these factors present significant obstacles to the development of practical perovskite applications.

1.2 Perovskite materials

The family of MPHs has a stoichiometry of ABX_3, where A is a monovalent organic or inorganic cation like Cs, methylammonium (MA) or formamidinium (FA); B is a divalent metal cation like Pb, Sn or Ge; X is halide anion including Cl, Br or I. The term “perovskite” originally refers to the crystal structure of $CaTiO_3$, and now is used for the chemical compound of a similar cubic crystal structure that consists of a network of corner-sharing BX_6 octahedra (Figure 3). By chemical engineering, the bandgap of perovskites can be easily tuned from 350 nm to 1000 nm which covers the entire visible spectrum.[24] Doping other chemicals such as small alkaline ions, polymer and organic spacer can further improve the optical properties of perovskite materials.[25]

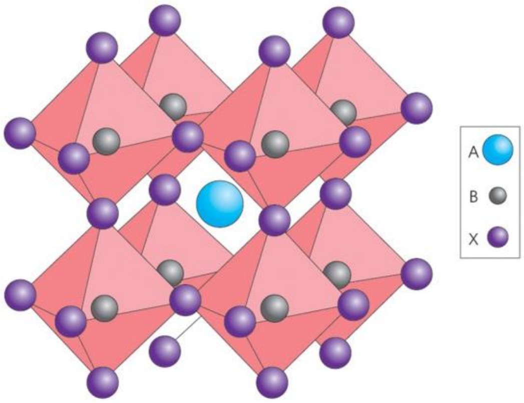

Figure 3 Perovskite crystal structure. The figure is reprinted with permission from ref [3]. Copyright 2014 Springer Nature.

The extraordinary optoelectronic properties of perovskites come from their crystal structure. Hybrid organic-inorganic halide perovskite materials have a general chemical formula as ABX_3. The A species exhibits 12-fold cuboctahedral coordination with X anions, occupying the interspace of an octahedral BX_6 framework. In the case of $[PbI_6]^{4-}$, the valence band maximum (VBM) is created by antibonding orbitals derived from the Pb(6s) and I(5p) atomic states, while the conduction band minimum (CBM) is formed by antibonding Pb(6p) and I(5s) orbitals.[4] These antibonding interactions have very small effective electron mass, comparable to holes' effective mass, resulting in high carrier mobility and ambipolar charge transport. The cubic crystal structure with high symmetry in perovskites leads to a direct bandgap. Additionally, the presence of lone pair electrons on the Pb s orbital leads to p-p electronic transitions from the valence band to the conduction band, which contributes to the material's exceptionally high optical absorption.

The Goldschmidt tolerance factor, t, has been widely utilized for predicting the stability of the perovskite structure. It relies solely on the ionic radii (r_i) of each ion (A, B, X). The value of t in the range of 0.8–1 indicates an ideal cubic perovskite structure:

:

$$t = \frac{r_A + r_x}{\sqrt{2}(r_B + r_x)}$$

Easy tunability and low fabrication cost are the two major advantages of perovskites. As mentioned above, perovskites have a general chemical formula of ABX_3, where all these components can be chemically tuned. Perovskite precursors can be prepared by solution methods, during which different components and additives can be mixed and doped into perovskites, then the perovskite crystal structure can be spontaneously formed under mild temperature annealing.[26] Co-evaporation and atomic layer deposition (ALD) are also available for perovskite layer synthesis.[27,28]

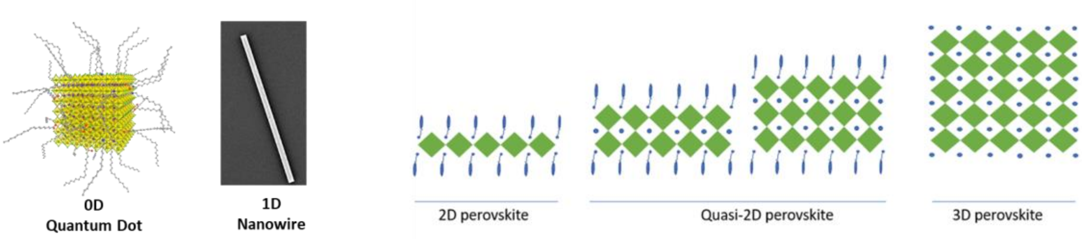

Eaton, Samuel, et al. *Proceedings of the National Academy of Sciences* (2016)

Figure 4 Perovskites with different dimensions.

Perovskite quantum dots (PQDs) are considered as 0D materials. They consist of a perovskite crystal core and organic ligand shell. The perovskite quantum dots are usually prepared by solution process with hot injection method or ligand assisted reprecipitation (LARP).[29,30] The size of quantum dots can be easily controlled by temperature and ligand concentration. Compared with inorganic quantum dots (like CdSe/ZnS and InP/ZnS), perovskite quantum dots have much lower fabrication costs but higher PLQY. Many literatures have reported perovskite quantum dots with PLQY around 100%,[31-33] making them promising candidates in display applications. Besides, the ligand shell structure of PQDs can act as the protective layer that prevents degradation from moisture and oxygen, thus PQDs are usually more stable than 3D perovskites.

1D perovskite nanowires can be synthesized by similar methods as PQDs. The self-assembled nanowires have perfect crystal facets and thus are intrinsically resonant cavities. Ultra-low threshold optically pumped perovskite lasers based on nanowires have been extensively studied.[14,21]

By adding organic molecules (spacers) into 3D perovskites, lower dimension perovskites (Ruddlesden-Popper type perovskites) can be obtained. Such kind of structure can be written with a general formula as $L_2(ABX_3)_{n-1}BX_4$, where L represents the spacer layer and n represents the number of monolayers between the spacers. By decreasing n from ∞ to 1, 3D, quasi-2D and 2D perovskites can be fabricated respectively, as shown in Figure 4.

Compared with 3D counterparts, quasi-2D and 2D perovskites have superior ambient stability. The hydrophobic spacer and the van der waals interaction between adjacent layers help prevent degradation from moisture and oxygen.[34] In the meantime, the layered structure of spacer/perovskite/spacer naturally formed a multi-quantum well structure. The QW structure has a dimension approaching the Bohr radius of electrons, thus it leads to strongly bound excitons. With higher bounding energy, excitons have a lower possibility of dissociation. This finally benefits the material's luminous efficiency.[35] Besides, 2D/quasi-2D perovskites also have better film morphology and lower surface roughness compared with 3D perovskites.

1.3 Perovskite carrier dynamics

One of the key aspects that make perovskites promising for optoelectronics is their efficient carrier dynamics. Carrier dynamics refers to the behavior of charge carriers in the material under the influence of external stimuli such as light or electric fields. Understanding and controlling carrier dynamics is crucial for optimizing the performance of perovskite devices.

Low-dimensional perovskites, such as quantum dots, 2D, and quasi-2D perovskites, exhibit unique chemical properties. These materials possess intrinsic quantum wells (QWs) that result in enhanced quantum confinement and dielectric confinement. Consequently, these features lead to a significant increase in the exciton binding energy. As the number of lead halide octahedral sheets increase from $n = 1$ (2D) to $n = \infty$ (3D), the exciton binding energy decrease, and excitons gradually disassociate by thermal energy. In general, carriers in low-dimensional perovskites are predominantly excitons, whereas 3D perovskites are dominated by free electron-hole pairs, as shown in Figure 5(a). This crucial distinction explains why low-dimensional perovskites exhibit significantly different photoluminescence and ASE behaviors when compared to their 3D counterparts.[36-38]

The carrier dynamics for excitons and free carriers are different. Here we use quasi-2D and 3D perovskite films as a comparison, as shown in Figure 5(b)&(c). For quasi-2D films, excitons dominate and their rate equation is expressed by:

$$-\frac{dn_x}{dt} = k_{ex}n_x + k_{bx}{n_x}^2$$

Where n_x is exciton density, k_{ex} is excitonic emission and k_{bx} is exciton-exciton annihilation (EEA) rate coefficient. The first-order term (excitonic emission) is radiative and the second-order term (EEA) is nonradiative. At low excitation power, the excitonic emission is fast and efficient, thus leading to higher PLQY for quasi-2D perovskites. However, as the excitation power increases, the exciton-exciton annihilation (EEA) process becomes more prominent and leads to a higher ASE/lasing threshold.

For 3D perovskites, the dynamics of free carriers are similar to other semiconductor and their rate equation is:

$$-\frac{dn}{dt} = k_1n + k_2n^2 + k_3n^3$$

Where n is the free carrier density, k_1, k_2 and k_3 are trap-assisted, bimolecular (radiative), and Auger recombination rate coefficients respectively. The PL intensity for 3D perovskites scale with the square of the excitation fluence, thus have a low PLQY and ASE/lasing threshold compared to quasi-2D perovskites.

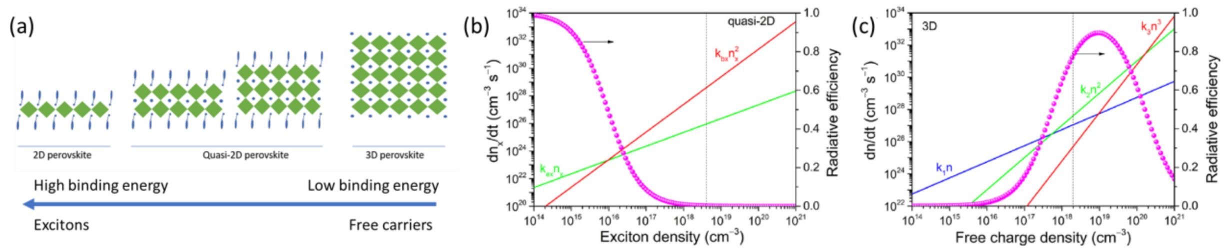

Figure 5 Perovskite carrier dynamics. (a) The binding energy and carriers in different dimensional perovskites. (b) &(c) Dependence of the carrier decay rates and radiative efficiencies of quasi-2D and 3D perovskite thin film. The figure is reprinted with permission from ref [39]. Copyright 2021 The Authors. Published by Elsevier Ltd.

Chapter 2. Perovskite light-emitting materials synthesis and study

During my research, different types of perovskites were explored and utilized for different applications. For color converters, perovskites need to have high converting efficiency and survive multiple photolithography processes, so perovskite quantum dots with high PLQY and high stability are preferred. For LEDs, perovskites should have high conductivity and thermal stability, thus quasi-2D perovskites are our major choices. For laser devices, a high radiative recombination rate under intense pumping is necessary, so 3D perovskites with dopants were applied.

In experiment practice, the quality of perovskite film is critical to devices' performance. Thus, special care and operations are needed during chemical synthesis. All chemicals need to be stored according to the safety data sheet (SDS) provided by the manufacturer, especially organic chemicals, which are mostly stored in the glove box to avoid oxidization. Certain chemicals need special treatment. For example, 18-crown-6 has a melting point of 42 ℃, once I observed it melted to liquid during summertime. Oleylammonium Iodide decomposes quickly and will be no longer usable after 6 months. DMSO and DMF solvents are hygroscopic and need to be sealed and stored in a glove box. To achieve the best performance for perovskite devices, all chemicals should be double-checked before use.

2.1 Perovskite 2D/quasi-2D/3D thin film

Perovskite thin films are usually deposited by a simple solution process. By mixing metal halide and organic halide chemicals in polar solvents, like DMF and DMSO, perovskite precursors can be obtained (Figure 6 (a)). Any spacers or dopant can be added into the precursor to easily tune perovskites' electrical, optical and chemical properties. The precursor is then spin-coated on the substrates in an anhydrous nitrogen-filled glove box to avoid phase degradation. Anti-solvent treatment and annealing process can both improve film quality.[40]

A recipe for synthesizing 0.2M quasi-2D perovskite, $(PEA)_{0.4}CsPbBr_3$), is listed here:

(1) Put a stir bar in a clean vial and transfer the vial into the glove box. Using a nitrogen gun to squeeze out the air from the vial.

(2) Weigh 127.68mg CsBr, 220.2mg $PbBr_2$, 48.48mg PEABr and 10.5 mg 18-crown-6 in vial. These chemicals are 0.6M in total.

(3) Add 3 mL DMSO into the vial and stir at 60 C for 2 h to guarantee sufficient dissolving.

(4) After cooling down, use a 0.45 μm PTFE filter with syringe to filter the precursor. Use a new vial to get the filtered precursor. The precursor will expire in two weeks because small perovskite nanocrystals will gradually crystalize and grow in the precursor.

(5) The perovskite precursor solution is spin-coated onto substrates at 3000 rpm for 60s with an acceleration speed of 1500 rpm/s. Afterward, the perovskite films were immediately annealed at 100 °C for 1 min to accelerate nucleation. The perovskite thin film shows strong photoluminescence under UV excitation, as shown in Figure 6 (b).

2.2 Perovskite quantum dot

Perovskites in the quantum dots (QD) form have high photoluminescence quantum yields (PLQYs) of up to 95%. Their narrow light-emitting peaks with an FWHM of about 20 nm are particularly attractive for high-quality light-emitting devices.[41] Perovskite quantum dots are typically formed from the reaction between metal halide and organic halide, and then self-organized into nano-crystal structures with the assistance of long-chain ligands. Most quantum dot synthesis depends on high temperature to control the crystallization speed and thus determines the QD size, and requires the inert gas environment to suppress perovskite degradation. Here we utilized a room-temperature ligand-assisted synthesis method to provide high-quality QD samples, shown in Figure 6 (c)&(d). Those quantum dots have a PLQY of up to 99.6% and stayed stable in the ambient environment for more than six months.

First, four kinds of precursors are obtained by constant stirring at 60 °C to get clear solutions:

(A) 0.1 M Cs_2CO_3 dissolves in octanoic acid (OTAc);

(B) 0.1 M PbBr2 and 0.2 M tetraoctylammonium bromide (TOAB) mixed and dissolved in toluene;

(C) 0.1 M ZnBr2 and 0.2 M TOAB mixed and dissolved in toluene;

(D) Didodecyldimethylammonium bromide (DDAB) dissolves in toluene with a concentration of 10 mg/mL.

The quantum dots are synthesized by mixing 600 uL solution D and 1800 uL solution B. Then 200 uL solution A is swiftly added into the mixture, forming a yellow precipitate (PQDs). After that, 600 uL of solution D and solution C are added to further passivate the PQDs. In the end, the PQDs are purified by several rounds of centrifuging, redispersing with toluene, and washing with ethyl acetate. The final products of PQDs can be dispersed in non-polar solvents, like toluene, hexane or heptane.

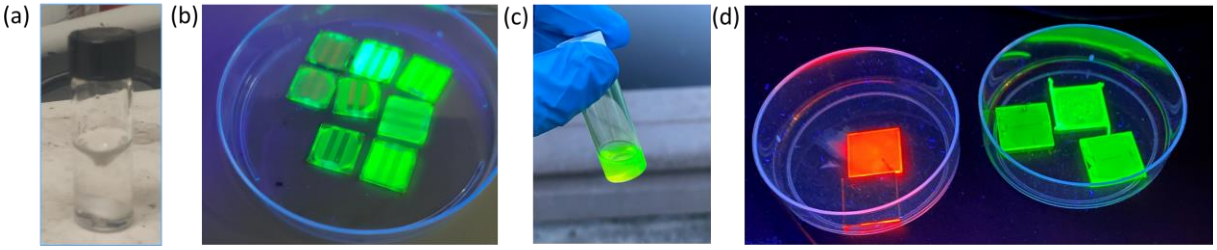

Figure 6 Perovskite materials. (a) perovskite precursor. (b) quasi-2D perovskite thin film under UV excitation. (c) perovskite quantum dot under daylight. (d) perovskite quantum dot films.

2.3 Quasi-2D Perovskite LEDs

Perovskite LEDs have been actively researched and developed as a potential alternative to traditional LEDs, offering advantages such as high color purity, tunable emission spectrum, and lower fabrication costs. To investigate the feasibility of perovskite lasers, we conducted an initial examination of perovskite LEDs, focusing on their electroluminescence and charge carrier transportation characteristics.

In our study, we synthesized quasi-2D perovskites using a mixed composition of CsPbBr3, PEABr, and 18-crown in a molar ratio of 1:0.4:0.07. The addition of the polymer 18-crown helped passivate the surface and reduce defects in the perovskite material.[42]

The LED is designed with a sandwich structure (glass/ITO/PEDOT:PSS/perovskite/TPBi/LiF/Ag), as illustrated in Figure 7(a). The transparent ITO is deposited on glass substrate with a thickness of 125nm. 40nm-thick of PEDOT:PSS is spun cast as the hole transporting layer. A 30nm-thick emission layer is prepared by spin-coating using perovskite precursors mentioned in the previous section. The sample is then baked at 100°C to accelerate perovskite crystallization. After that, 35nm TPBi (hole transporting layer), 1.5nm LiF (helps lower the work function of silver electrode) and 100nm silver electrode are deposited on the sample in sequence by evaporation with shadow masks. The red box in Figure

7(a) indicates the working area, where ITO and silver electrodes are overlapped. The as fabricated perovskite LED shows a very high brightness when working under voltage bias (shown in Figure 7(b)).

The energy diagram of each layer is shown in Figure 7(c). Since the emission layer is consist of different phases of perovskites, their band edges are not labeled. By applying voltage, electrons and holes are injected from Ag/LiF electrode and ITO electrodes, respectively. TPBi and PEDOT:PSS are hole transporting layer and electron layer, that can transport one carrier while blocking the other. By controlling the thickness of these layers, a proper balance between the injection of electrons and holes can be achieved. This balance is crucial for efficient charge transport and recombination within the perovskite layer, leading to improved external quantum efficiency (EQE) of the device. Tailoring the thickness of the hole transporting and electron layers helps optimize the charge carrier injection and transport, thereby enhancing the overall performance of the PeLED.

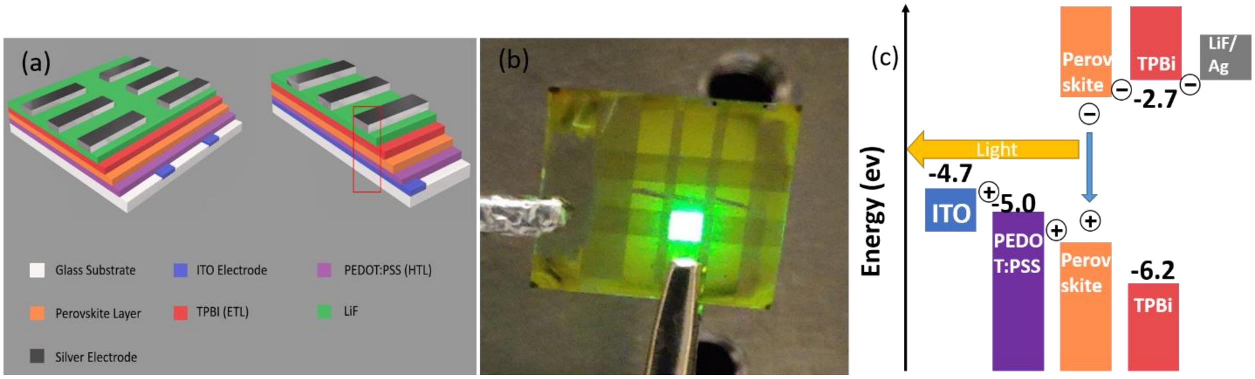

Figure 7. Perovskite LEDs. (a) LED structure 3D model. (b) LED EL. (c) Energy diagram of LED structure.

The external quantum efficiency (EQE) is a crucial parameter in LEDs. It quantifies the efficiency of converting injected charge carriers into emitted photons. EQE is defined as the ratio of the number of emitted photons (Nphoton) to the number of injected charge carriers (Nelectron). The EQE can be calculated via

$$\mathrm{EQE} = \frac{N_{photon}}{N_{electron}} = \frac{N_{photon}}{I/e} = \frac{e}{hv} \cdot g \cdot \frac{P}{I}$$

Where I is the current flowing through the LED device, P is the emitted power measured by a photodetector. Since PeLEDs can be considered as Lambertian light sources, we can introduce a geometry factor, g, to calibrate the photodetector, which is expressed by

$$g = \frac{r^2 + L^2}{r^2}$$

Where r is the diameter of the detector, L is the distance between the detector and LED surface.[43]

Then the luminance (L) can be calculated by:

$$L = \frac{683 \times P \times g \times V(\lambda)}{\pi A}$$

Where V(λ) is the luminous function representing the average spectral sensitivity of human visual perception of brightness, and A is the device area.

The electroluminescence (EL) properties of perovskite LEDs are measured and the results are shown in Figure 8. The LEDs show a turn-on voltage of about 2.9V with a maximum EQE of 10.9% and a luminance of 24700 cd/m^2.

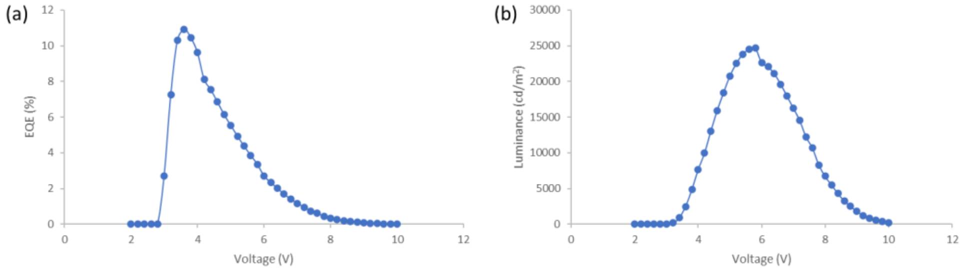

Figure 8. Perovskite LED performance. (a) EQE vs voltage curve. (b) Luminance vs voltage curve.

2.4 Perovskite LEDs with hole array structure

Perovskite LEDs face challenges in achieving high external quantum efficiency (EQE) due to the material's large refractive index (2.3-2.7).[7,44] A large portion of the light will be trapped in waveguide mode and thus do not contribute to the EQE. On the other hand, due to the small Stokes shifts of perovskites, photon recycling plays an important role in the quantum yield measurement. Methods have been proposed to maximize perovskites' photon recycling and thus increase the efficiency, e.g. low -index grids, [51] textured substrate[45] and confined electrodes with associated parasitic absorption.[46]

Here we successfully demonstrated a green pixelated perovskite LED with a hole array. Figure 9(a) schematically depicts the structure of PeLEDs with hole arrays. To avoid the current shunt path between the cathode and anode, an insulating layer (SiO2) was deposited and patterned with 50/100 μm holes on the ITO layer, shown in Figure 9 (b)(c). The holes also play as current apertures to help mitigate Joule heating.[47] While working, the current is confined in the hole area and the surrounding perovskites work as a heat sink and photon recycle gain material.

Figure 9(d)-(f) show the performance of PeLEDs fabricated in the same batch. A plain LED with no hole array is used as a reference. The reference PeLED, 50 μm hole array PeLED and 100 μm hole array PeLED showed a maximum EQE of 6.64%, 7.57% and 7.54% respectively, indicating a 14% increase. The current focusing effects are more obvious than EQE improvement. The maximum luminance of the hole array LEDs showed about 2.8 folds over the reference device at around 5.8 volts, as shown in Figure 9(e).

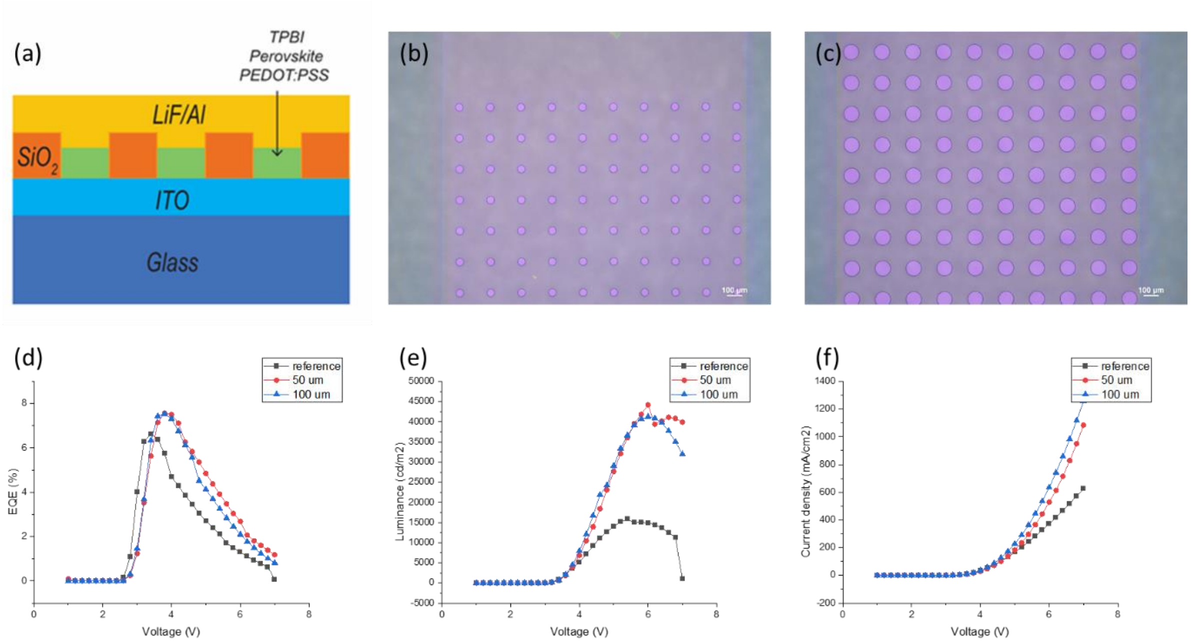

Figure 9. PeLEDs with hole arrays. (a) Schematic structure of pixelated PeLEDs. (b)&(c) 50 µm and 100 µm SiO2 hole array on ITO layer. (d)-(f) The performance comparison between reference and PeLEDs with current aperture structure over EQE, luminance and current density.

Chapter 3. Perovskite optically pumped lasers with $MAPbBr_3$

Adapted with permission from:

Chang, C., Shi, Y., Zou, C., & Lin, L. Y. (2023). MAPbBr3 First-Order Distributed Feedback Laser with High Stability. Advanced Photonics Research, 4(1), 2200071. Copyright 2022 The Authors. Advanced Photonics Research published by Wiley-VCH GmbH

3.1 Abstract

A green-emitting perovskite first-order distributed feedback (DFB) laser based on methylammonium lead bromide ($MAPbBr_3$) with high stability is demonstrated for the first time. The laser achieved stable lasing at 550 nm with a full width at half maximum (FWHM) of 0.4 nm. A low lasing threshold of 60 μJ cm^{-2} under nanosecond pulsed excitation and 3.1 μJ cm^{-2} under femtosecond pulsed excitation were observed, showing a much lower lasing threshold compared with the second-order DFB cavities we fabricated on the same substrate. By optimizing antisolvent treatment and encapsulating with PMMA, the laser lifetime, moisture resistance, lasing threshold and intensity were significantly improved. The lasers were fabricated with a CMOS-compatible process, thus offering promising potential for integrated photonic devices.

3.2 Introduction

In this part, we demonstrated a green-emitting perovskite 1st-order DFB laser with a low lasing threshold, narrow FWHM, high resistance to moisture and long-term stability. The laser was fabricated on a silicon wafer with a CMOS-compatible process. Figure 10 shows the SEM images (Figure 10(a) and (b)) and a schematic (Figure 10(d)) of the device. To facilitate detection of the laser output, 2^{nd}-order DFB gratings are utilized at both ends of the 1^{st}-order DFB grating to couple the laser light out vertically. Those edge 2^{nd}-order DFB gratings were not capable of generating lasing but only facilitated light extraction. Figure 10(c) shows the dark field image of the 1^{st}-order DFB laser under operation. Upon nanosecond pulsed laser excitation which illuminates the 1^{st}-order DFB grating area only, the laser achieved a narrow FWHM of 0.4 nm and a threshold of 60 μJ cm^{-2}. This threshold value is about 60% lower than the 2^{nd}-order DFBs with the same design. The laser also shows long-term stability and moisture resistance with the encapsulation of a PMMA layer. During a 4-hour pumping process, the emission spectrum shows no change in FWHM and minor degradation in peak intensity.

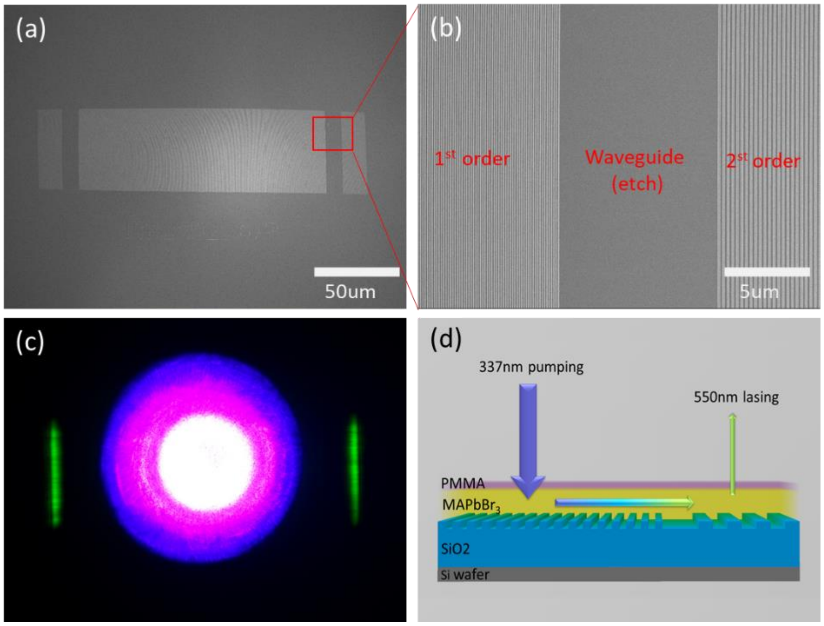

Figure 10. Optically pumped perovskite laser. (a) SEM image of the 1st-order DFB grating for the perovskite laser with (b) a 2nd-order DFB grating area for output coupling. A waveguide region without gratings separates the output-coupling grating from the 1st-order DFB resonator. (c) Dark-field optical microscope image of the 1st-order perovskite DFB laser under operation. The image shows the pumping light illuminating the 1st-order DFB grating region, and the green emission coupled out of the 2nd-order DFB gratings at both ends. (d) Schematic of the perovskite 1st-order DFB laser.

3.3 Device design and fabrication

3.3.1 DFB cavity design

The DFB gratings are fabricated by electron-beam lithography (EBL) on a silicon dioxide (SiO_2) layer thermally grown on a silicon wafer, shown in Figure 12. The DFB grating designs are determined by Bragg condition:

$$q\lambda_{Bragg} = 2n_{eff}\Lambda$$

where q is the diffraction order (q=1 for 1st order and q=2 for 2nd order); λ_{Bragg} is the Bragg wavelength; n_{eff} is the effective refractive index; Λ is the grating period.

For 1st-order DFB lasers, the lasing direction is in the plane of the gratings. This edge-emitting behavior requires cleaving the device chip to characterize the laser output. However, cleaving the chip brings risks of damaging the soft perovskite layer, and compromises repeatability because spin-coating perovskites results in a rough and thicker edge. Therefore, for testing our devices, a few dozen periods of 2nd-order DFB gratings are incorporated at the end of the device for efficient vertical outcoupling of light, as shown in Figure 10(a). The 2nd-order DFB gratings are separated from the 1st-order DFB grating by a channel waveguide structure through the etching part of the SiO_2 layer. By avoiding cleaving the chips, the substrates can be reused and the experimental results were highly repeatable. Figure 12 (a) and (b) show that high-quality gratings with a period of 140 nm and 280 nm were obtained by EBL for 1st-order and 2nd-order DFB, respectively.

To show that the 2nd-order DFB gratings at the edge had no influence on our 1st-order DFB laser measurement, we fabricated devices that only have the edge gratings (Figure 11(b)). The origin 1st-order DFB grating area was removed by etching away the entire region, so perovskites will fill the trench and form a waveguide. Under the same excitation (152 μJ cm^{-2}), the emission spectrum of these two devices as well as ASE is shown in Figure 11(c). It shows that the edge 2^{nd}-order DFB gratings were not capable to generate lasing but only facilitated light extraction.

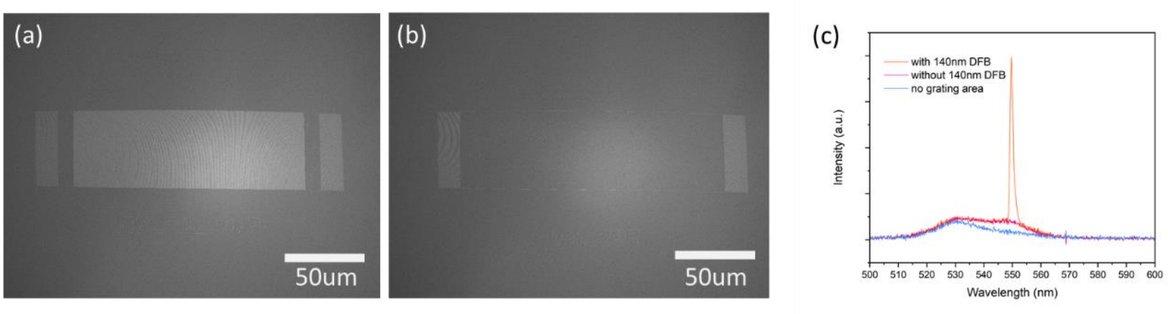

Figure 11 Comparison between (a) a 1^{st}-order DFB laser with 2^{nd}-order DFB gratings for output coupling and (b) a device with a waveguide and the 2^{nd}-order DFB gratings at the edge. (c) The output spectrum of the device shown in (a)(b) and ASE.

$MAPbBr_3$ precursor was spin-coated on the DFB grating-patterned SiO_2/Si substrates with the help of antisolvents. The differences in polarity, miscibility and boiling points of the antisolvents lead to significant variances in the perovskite films.[40,48] We compared several different antisolvents and found ethyl acetate could best improve the laser performance, which will be discussed later.

To improve laser stability, a thin layer of PMMA was spin-coated on top of the perovskite layer. The lasing mode profile in the DFB cavity is strongly dependent on the layer thickness of the gain material, so the thickness of the perovskite layer, the PMMA layer and the grating depth were carefully optimized to achieve an effective index that matches the grating period, thus to achieve the desired laser output wavelength.

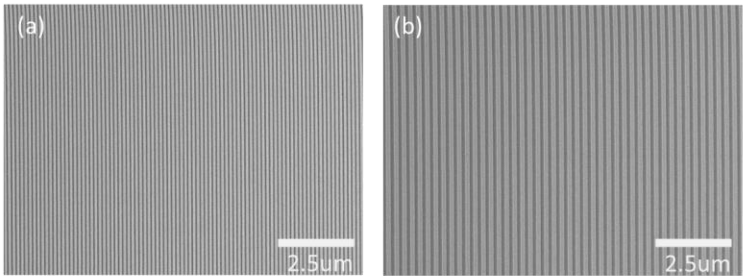

Figure 12. SEM image of (a) 1st-order DFB gratings and (b) 2nd-order DFB gratings.

To find the optimized DFB cavity design, a dozen of FDTD simulations were performed. The dependence of lasing peak wavelength and quality factor on the layer thickness can be found in Table 2.

perovskite thickness [nm]	PMMA thickness [nm]	Grating period [nm]	Quality factor	Peak wavelength [nm]
110	50	140	2029	509.1
120			1607	516.9
130			1274	524.0
135			1135	527.2
140			1007	530.0
150			809	536.0
135	0	140	1460	521.2
	30		1221	525.7
	50		1135	527.2
	80		1063	528.3
	50	145	1162	543.2

		150	1186	559.2
		155	1208	574.9

Table 2 Simulation results for the relationship between each layer's thickness, quality factor and peak wavelength. The values are different from actual devices due to fabrication variance and simulation resolution.

The mode profile distributions in the substrates are obtained by simulations. All electric field magnitudes are already unified to make comparisons. The blue, yellow and purple parts are SiO_2, perovskites and PMMA respectively.

Figure 13(a)-(c) show gratings with no PMMA encapsulation and a perovskite layer of 110 nm, 135 nm and 150 nm respectively. It can be seen that a thicker perovskite layer increases mode confinement. However, since the grating depth is fixed to 60 nm, the thicker perovskite layer, the less optical feedback there will be. This is in accordance with the Q-factor data shown in Table S1. In the meantime, to obtain a uniform perovskite film with good coverage and enough optical gain, the perovskite layer cannot be too thin.

Figure 13(d)-(f) show the influence of PMMA layer thickness over the mode profile. PMMA is absorptive and forms an index gradient between perovskites and air, so increasing PMMA thickness will significantly decrease mode confinement and quality factor. However, a thick PMMA layer is essential for good encapsulation.

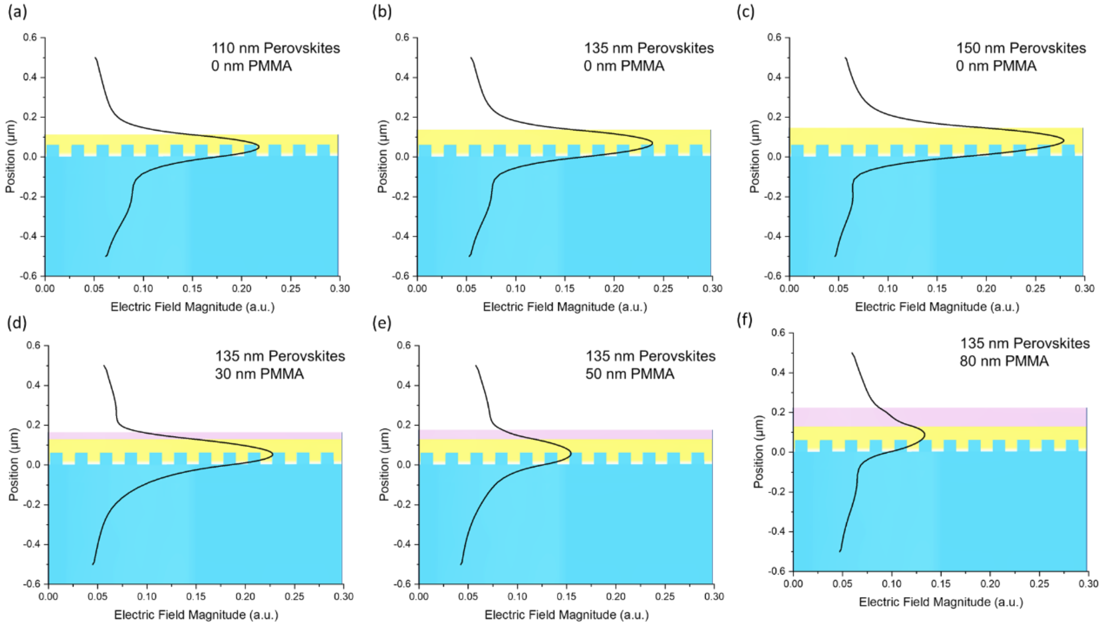

Figure 13 Mode profile distribution in the grating area.

3.3.2 Device fabrication and characterization

Materials: MABr (>99.5% purity) was purchased from Ossila. $PbBr_2$ (99.9%, metal basis), PMMA (~120,000 MW) and Dimethyl sulfoxide (DMSO, anhydrous) were purchased from Sigma Aldrich. DisCharge (2x) was purchased from DisChem.

DFB gratings fabrication: Silicon substrates with 2 µm wet thermal oxide were cleaned by ultrasonication using detergent, acetone, isopropanol and DI water, followed by plasma cleaning at 150W for three minutes. A 110 nm layer of ZEP520A Ebeam lithography resist was spin-coated on the substrates and annealed at 180 ℃ for three minutes. Then a DisCharge layer was spin-coated on the resist at 4000 rpm. Electron beam lithography was performed to draw grating patterns on the resist layer using a JBX-6300FS system (JEOL) with an optimized dose of 185 $\mu C/cm^2$. After the exposure, the substrates were submerged in water for one minute to strip the DisCharge. Amyl Acetate was used to develop the patterns at room temperature. The patterned resist layer is used as the etching mask in an Inductively Coupled Plasma (ICP) fluorine etcher to etch 60 nm of silicon dioxide. Finally, the substrates were heated in N-Methyl-2-pyrrolidone (NMP) at 90 ℃ overnight to strip the resist.

Solutions synthesis: The green perovskite precursor was obtained by mixing 0.84 M MABr and 0.8 M $PbBr_2$ (MABr : PbBr = 1.05 : 1) in DMSO. The precursor was heated at 60 °C for 12 h with constant stirring. After cooling to room temperature, the precursor was filtered with 0.45 µm PTFE filters. The encapsulation layer is prepared by dissolving 20 mg of PMMA in 1 ml of toluene and stirring for a sufficient time.

Device fabrication: The silicon substrates with DFB gratings were cleaned as previously described. Then the substrates were treated with ultraviolet plasma cleaning to increase wettability. The precursor solution of $MAPbBr_3$ was spin-coated on the substrate at 3000 rpm for one minute in a nitrogen-filled glove box. 200 µl of antisolvent was dropped onto the substrate during spin-coating to accelerate nucleation. Then the substrates were baked at 60 °C for 10 minutes. PMMA in toluene was spin-coated on the perovskite layer as an encapsulation layer and then annealed for another 10 minutes.

ASE and lasing measurement: For both ASE and lasing measurement, the samples were pumped by a nanosecond nitrogen laser (337 nm, 20 Hz, 3.5 ns pulse width; NL 100, Stanford Research System) with a micro-PL system. The pump fluence was tuned by a continuously variable ND filter. Both the excitation light and PL were vertically coupled in/off the sample. A cascaded 4-f imaging system in conjunction with a 450 nm longpass filter was used to collect the emission before a spectrometer (Thorlabs CCS100) and a CCD camera.

3.4 Results and discussion

3.4.1 ASE and lasing performance

A nanosecond pulsed laser with 337 nm wavelength, 20 Hz repetition rate and 3.5 ns pulse width was used as the pumping source unless otherwise specified. All measurements were done at room temperature in an ambient environment.

The ASE was obtained by pumping the area without DFB gratings. Figure 14(a) and (b) show the evolution of the ASE spectrum versus pump fluence. At low excitation, the photoluminescence (PL) spectrum shows an FWHM of 21 nm around a 530 nm emission peak. After the pump fluence is increased to around 400 μJ cm^{-2}, the FWHM is reduced to 2 nm and the emission peak shifts to 550 nm, both indicating the onset of ASE. The red shift is attributed to the transition from a higher-energy bound exciton state (PL) to a lower-energy bound exciton state (ASE).[49] Under high pump fluence, the higher-energy state serves as the optical pump for the lower-energy state, thus the ASE emission at 530 nm dominates.

We then moved the pump light to the 1st-order DFB grating region and performed the measurements again. Figure 14(c) and (d) clearly indicate lasing of the perovskite laser. The emission spectrum shows a steep drop in FWHM once the pump fluence reaches a lasing threshold of ~60 μJ cm^{-2}. The narrow FWHM of 0.4 nm corresponds to a high lasing quality factor over 1300. We also fabricated 1st-order DFB gratings with different periods ranging from 138 to 144 nm. The emission spectra of the perovskite lasers with these DFB gratings are shown in Figure 14(e). The lasing wavelength is tuned from 546.9 to 556.8 nm, corresponding to the grating period change which affects the effective refractive index as well.

To compare the lasing threshold of 1st-order DFB lasers with 2nd-order DFB lasers, we fabricated both 1st- and 2nd-order DFB gratings on the same substrate with the same processing conditions. Lasing thresholds of 69.5 μJ cm^{-2} for the 1st-order DFB laser and 168.6 μJ cm^{-2} for the 2nd-order DFB laser were observed (Figure 14(f)), which is in accordance with the theory that the lasing threshold for 1st-order DFB lasers should be reduced by a factor of 2 compared to the 2nd-order DFB lasers.[50]

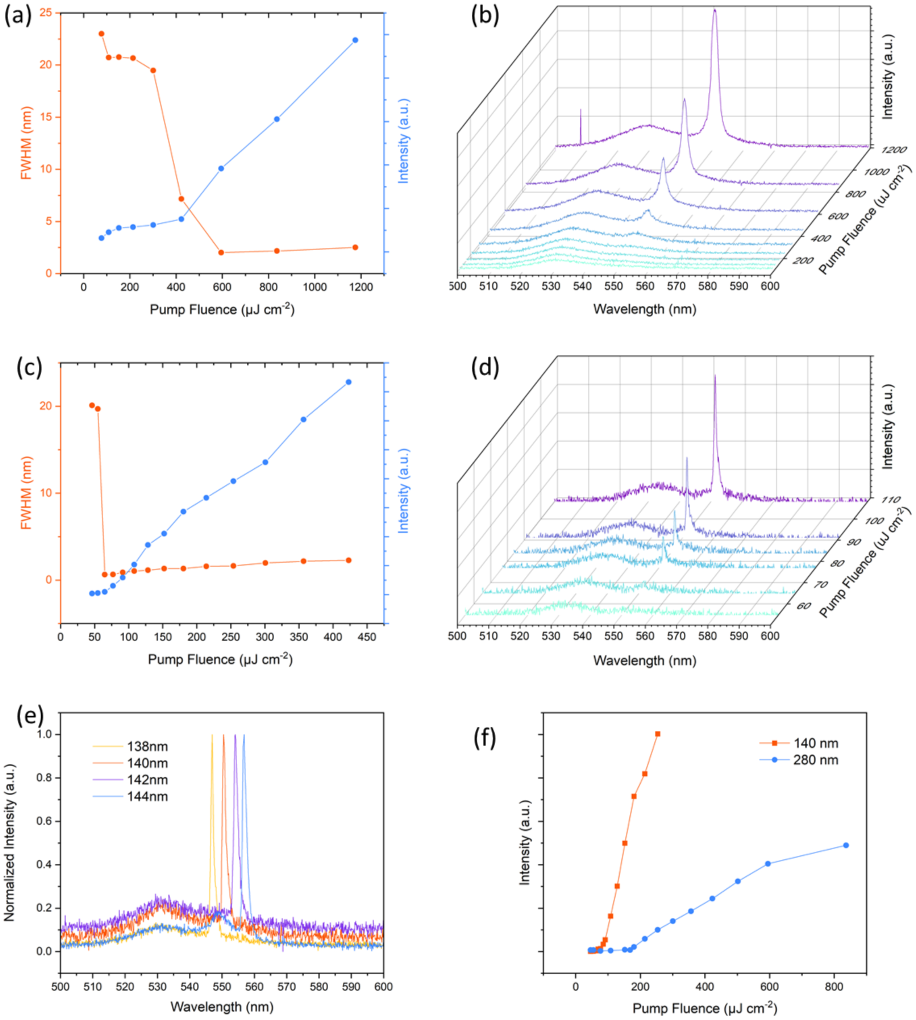

Figure 14. ASE and lasing properties. (a) FWHM and ASE intensity as a function of pump fluence. (b) Evolution of the ASE emission spectrum versus increasing pump fluence. (c) FWHM and laser output intensity as a function of pump fluence. (d) Evolution of emission spectra under different pump fluences. (e) Dependence of the lasing peak wavelength on the grating period of 1st-order DFB lasers. (f) Comparison between the laser output intensity of 1st- and 2nd-order DFB lasers.

3.4.2 Antisolvent treatment

The antisolvent method has been widely used for preparing high-quality, low-defect perovskite films in the application of solar cells, photodetectors and LEDs.[40] Common antisolvents for $MAPbBr_3$ are chlorobenzene (CB) and toluene (Tol) due to their insolubility of perovskites and miscibility with the precursor solvent (DMSO/DMF). The antisolvents are added during spin-coating right before perovskite crystallization. During the process, antisolvents mix with the perovskite precursor, extract the precursor solvent and form local supersaturation for perovskites, forcing the material to quickly recrystallize.[48]

Figure 15(a) shows the light-in versus light-out characterization results (L-L curve) for 1st-order perovskite DFB lasers fabricated using different antisolvents. The lasing thresholds for EA, MA, TOL and CB-treated devices are around 60, 95, 110 and 147 $\mu J\ cm^{-2}$, respectively. In the high pump fluence region, the laser intensity for MA, TOL and CB-treated devices are similar due to saturation, whereas the EA-treated device shows twice the intensity of the others. Figure 15(b) presents the lasing spectra of devices with $MAPbBr_3$ films using different antisolvents under nanosecond pulsed pumping with a pump fluence of 152 $\mu J/cm^2$, the peak intensity and wavelength clearly vary. Figure 15(c) shows the film morphology and surface roughness of each device. All devices have a smooth and glossy surface except the hexane-treated sample, where no lasing or amplified spontaneous emission (ASE) was detected due to high film roughness.

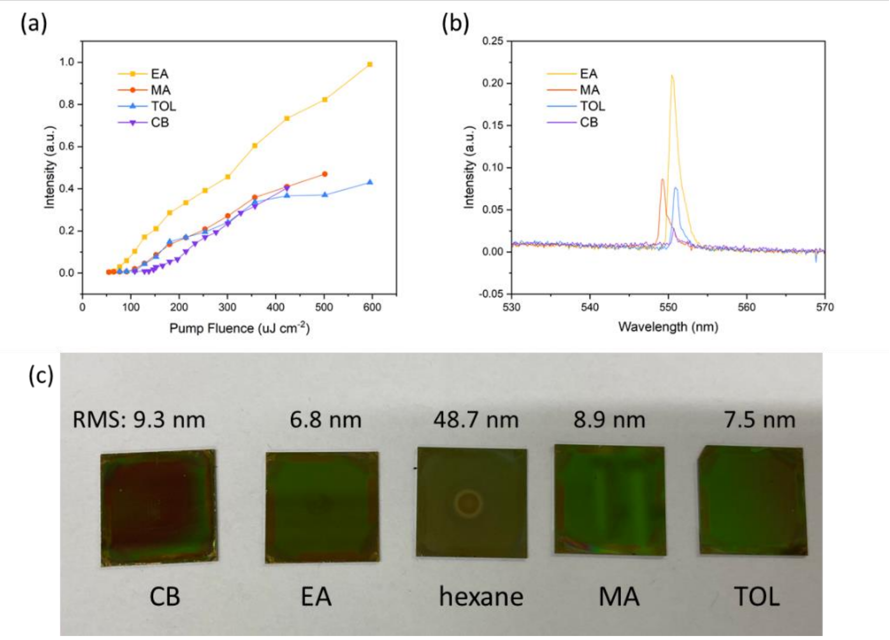

Figure 15. (a) First-order perovskite DFB lasers were fabricated using different antisolvents. (a) L-L curve and (b) laser emission spectrum under 152 μJ cm^{-2} nanosecond pulsed pumping. (c) Images of laser samples using different antisolvents with their surface roughness.

To obtain more reliable and statistically significant results, the lasing thresholds of multiple devices, fabricated in the same batch, were measured (shown in Figure 16). The observed trend in lasing thresholds for different antisolvents aligns with the findings presented in the research paper. Statistical analysis of the data reveals that ethyl acetate (EA) exhibits the smallest variance, while toluene (TOL) exhibits the largest variance. This discrepancy can be attributed to the varying durations that antisolvents remain in contact with the perovskite film during the fabrication process. EA and methyl acetate (MA) have shorter contact times of less than 0.3 seconds, whereas TOL has a longer contact time exceeding 1 second. This difference in contact duration may influence the speed and uniformity of perovskite crystallization, thus impacting the lasing thresholds observed.

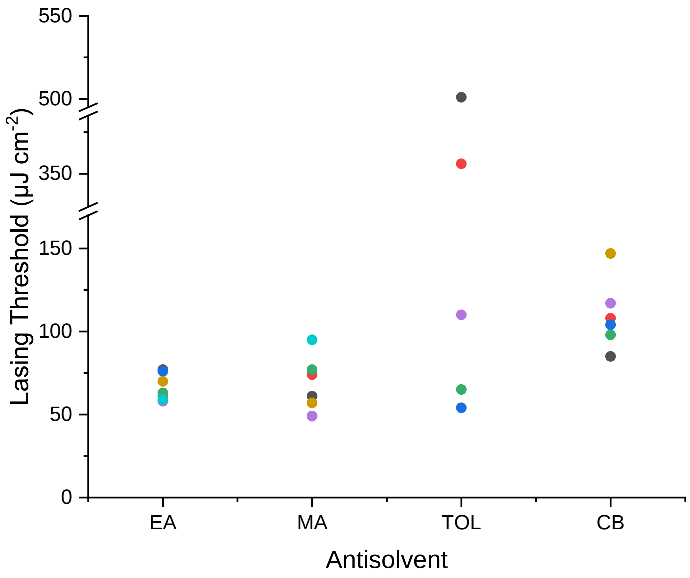

Figure 16 Lasing threshold vs antisolvent type.

To analyze the effects of antisolvents on the photoluminescence (PL) properties, the PL spectra and PL lifetimes of the samples were measured, and the results are presented in Figure 17.

The PL spectrum was obtained by a 405 nm CW laser, with a pumping intensity of 420 mW cm^{-2}. The recombination dynamics of perovskite films treated with different antisolvents would affect the lasing threshold. The charge carrier dynamics can be described with the following equation:

$$-\frac{dn(t)}{dt} = k_1 n + k_2 n^2 + k_3 n^3$$

Where n is the charge carrier density, t is the time, k_1 is the monomolecular recombination rate (a trap-assisted Shockley-Read-Hall recombination), k_2 is the bimolecular recombination rate and k_3 is the Auger recombination rate.

Under steady-state excitation, the PLQY (η(n)) for 3D perovskites is given by:

$$\eta(n) = \frac{k_2 n}{k_1 + k_2 n + k_3 n^2}$$

To lower the lasing threshold, we expect small k_1, k_3 and large k_2. In the high carrier density region (at the lasing stage), only small k_3 and large k_2 are particularly required as k_1 almost only affects the PLQY at low carrier density.

As shown in Figure 17(a), EA-treated films show the highest PL peak intensity at low excitation intensity, indicating the defect density of EA-treated films is the lowest among the four kinds of films, which also leads to the smallest k_1.

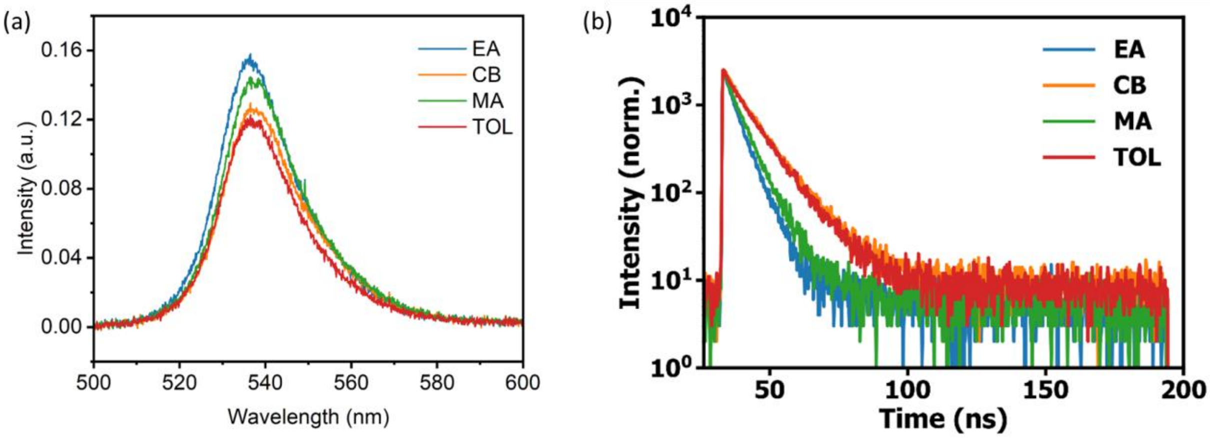

Figure 17 Perovskite films' PL and PL lifetime.(a) PL spectrum for perovskite films processed by different antisolvents. (b) PL lifetime measurement for perovskite films processed by different antisolvents.

The TRPL data in Figure 17(b) could be fitted by single-exponential decay well. PL lifetime measured for perovskite films processed by different antisolvents:

EA: 4.8 ns

CB: 9.4 ns

MA: 5.9 ns

TOL: 9.1 ns

The measurements are performed with a fluorescence lifetime spectrometer (PicoQuant, FluoTime 100, PicoHarp 300). Laser wavelength 405 nm, pulse width 70-90 ps, repetition rate 5 MHz. Considering the radiative recombination in 3D perovskites is mainly contributed from bimolecular recombination under picosecond laser pumping, the PL lifetime is approximately given by:

$$\tau_{rad} = \frac{1}{k_2 n}$$

The EA-treated films have the lowest PL lifetime, indicating the radiative bimolecular recombination rate (k_2) of EA-treated films may be the largest among the four kinds of films. That’s also why EA-treated films have the lowest lasing threshold.

3.4.3 Laser stability

Solving the stability issue of solution-processed perovskite lasers is still a key challenge. It is well known that perovskite materials degrade due to the chemical reaction with oxygen and moisture easily. Especially under the condition of high-power pumping, the accumulated joule heating accelerates the decomposition process, thus decreasing the laser performance. Ligand-modification for perovskite QDs,[51,52] hydrophobic organic layer engineering[53], and perovskite QD-embedded polyacrylonitrile[54] have all been proven to be effective methods to prolong the laser’s lifetime by isolating the perovskite gain materials from the air.

Here we show that with a thin layer of PMMA on top of the perovskite layer, the device performance and lifetime can be significantly improved. To compare the performance of the devices with and without PMMA encapsulation, we excite the lasers at a pump fluence of $2P_{th}$, where P_{th} is the lasing threshold, using the nanosecond pulsed laser. As shown in Figure 18(a), the unencapsulated device's output intensity quickly dropped to 60% of the initial value after about 10 minutes. The device encapsulated with PMMA showed stable lasing for 4 hours (288000 laser shots) with almost no FHWM broadening (Figure 18(a) and (b)). The laser output spectra in Figure 18(b) also shows that the laser peak intensity maintained ~82% of its initial value after 4 hours with a minor blue shift of ~0.3 nm. In contrast, the unencapsulated device only maintained 35% of the initial intensity and emission peak blue-shifted 1.7 nm (Figure 18(c)). It is interesting to notice that there is a slight intensity increase in the first 5-20 minutes of pumping for the encapsulated device. The increase wasn't very obvious for the unencapsulated device due to quick degradation. The phenomenon is also observed in similar works.[18,55,56] This may be due to the heating and recrystallizing of perovskites under optical pumping that smoothens the surface.

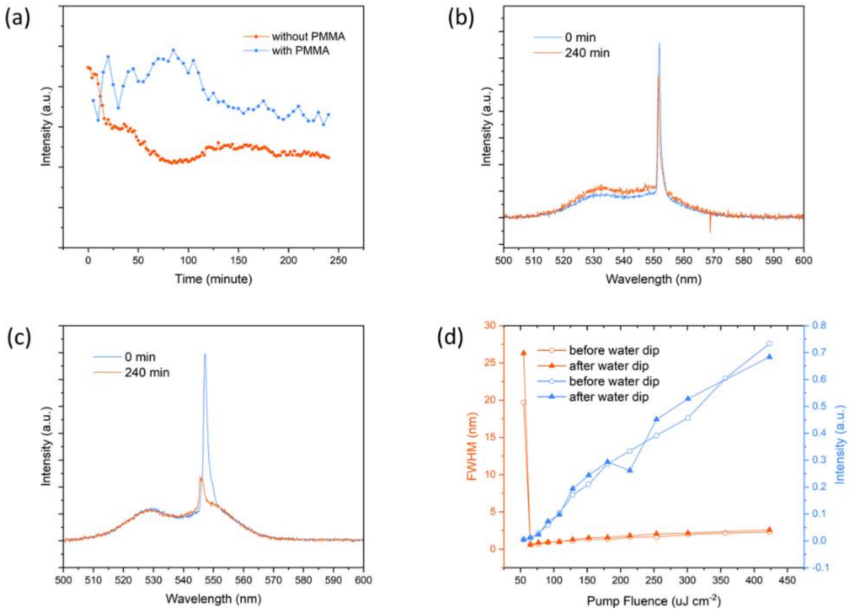

Figure 18. Perovskite laser's stability test. (a) Laser intensity over time under optical pumping at twice the lasing threshold. The lasing spectrum of (b) the PMMA-encapsulated device and (c) the unencapsulated device at the beginning and the end of the 4-hour measurement. (d) Laser performance before and after dipping into the water.

To accelerate the degradation effect from moisture, we dipped the device in water briefly and then compared its performance in FWHM and L-L characteristics (Figure 18(d)). The performance was almost identical before and after the dip, showing the PMMA layer provided sufficient protection against moisture. The perovskite layer in devices without PMMA encapsulation dissolved immediately in water, therefore further testing was not possible for these devices.

The samples used to compare 1st- and 2nd- order DFB lasers were stored in the air for a week and measured again. The lasing thresholds for first-order DFB laser before and after the storage were 69.5 and 64.9 μJ cm^{-2}, as shown in Figure 19.

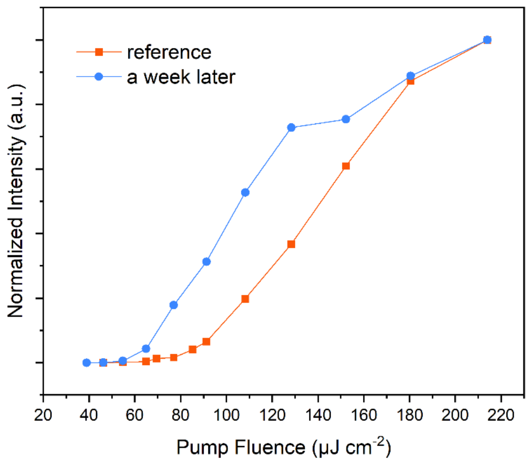

Figure 19 LL-curve for a 1st-order perovskite DFB laser measured a week later.

Some self-healing effects were also observed during laser operation. The perovskite laser output and PL intensity over time are shown below. The DFB laser has a lasing threshold of 55 μJ cm^{-2}. The pumping fluence is 130 μJ cm^{-2}, a little bit higher than twice the threshold. After pumping for 15 minutes, the pumping laser was turned off for two minutes. Figure 20 clearly shows the lasing intensity increases in the first two minutes and then gradually decreases. After the two minutes of cooling down, the lasing intensity is restored and the process is repeated. In the meantime, the PL intensity remains the same during the entire measurement. This indicates some more complicated mechanics besides heating and recrystallization are involved, e.g. thermal effects related lasing death. A more detailed investigation is required to further reveal the lasing mechanics for perovskites.

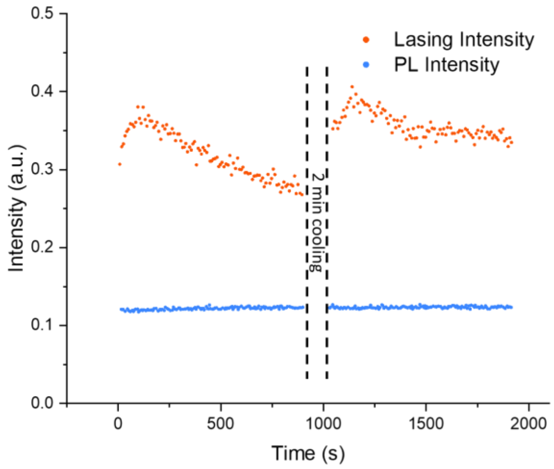

Figure 20 Lasing and PL output intensity versus time.

3.5 Conclusion

In summary, we designed, fabricated and optimized 1st-order DFB lasers based on $MAPbBr_3$, which shows around a 60% decrease in lasing threshold compared with 2nd-order DFB lasers. Utilizing ethyl acetate as the antisolvent, the lasing threshold was reduced significantly to 60 μJ cm^{-2} under nanosecond pulse pumping, and the optical output intensity was substantially higher than that of lasers treated with other antisolvents. Laser emission FWHM as narrow as 0.4 nm was achieved. The peak wavelength can be tuned from 546.9 nm to 556.8 nm by changing the 1st-order DFB grating period. With a thin PMMA layer encapsulation, the laser performance and stability can be greatly improved. The results demonstrate the promising prospect of perovskite DFB lasers in filling the green gap of semiconductor lasing sources for integrated photonics.

Chapter 4. Ultralow-threshold quasi-CW lasing from FAPbBr3 perovskite first-order DFB laser

Adapted with permission from:

Chang, Cheng, and Lih Y. Lin. "Ultralow-threshold quasi-CW lasing from FAPbBr3 perovskite first-order DFB laser." Nanotechnology 34.17 (2023): 175201. Copyright 2023 IOP Publishing Ltd

4.1 Abstract

To pursue electrically pumped lasers, we need to reduce optically pumped perovskite laser's lasing threshold. Here we report a quasi-CW pumped ultra-low ASE/lasing threshold formamidinium lead bromide ($FAPbBr_3$) laser. The laser achieved stable lasing at 555 nm with a full width at half maximum (FWHM) of 0.6 nm, showing a low lasing threshold of 22.6 μJ cm^{-2} under 3.5 nanosecond quasi-CW excitation at room temperature. The material also showed an ultra-low ASE threshold of 46 μJ cm^{-2} under the same pumping condition. Through polymer doping, we showed that the material's performance can be improved by increasing bimolecular recombination rate with reduced grain size.

4.2 Introduction

Metal-halide perovskites are promising solution-processed gain materials for low-cost on-chip lasers in integrated photonics. Ever since the first demonstration of perovskite lasers in 2014, many works have revealed the vast possibilities for perovskites. Xing, et al. demonstrated tunable ASE from spin-coated polycrystalline $MAPbX_3$ films (X = Cl, Br, I) that cover the visible spectrum, including the "green gap".[10] After that, Yakunin, et al. showed that ASE and lasing can be achieved at room temperature.[30] Since perovskites can be dissolved and damaged in most lithography developers, people used self-assembled perovskite single crystals, nanowires and nanoplates as feedback cavities and achieved lasing.[11,14,21,57,58] Despite the unstable nature of perovskite materials, multiple types of human-designed feedback cavities (DFB cavities, VCSEL, photonic crystal cavity, etc.) have been combined with perovskites and built up the broadways to integrated perovskite devices.[16,19,59,60]

Like all other organic semiconductor materials, LEDs and optically pumped perovskite lasers have been well developed, but electrically pumped perovskite lasers are still a long-standing challenge. However, the successful demonstration of organic polymer lasers pointed out a possible direction.[61] For perovskite laser diodes, there are several primary challenges to be solved: (a) incorporating high gain perovskites with optical feedback structure to achieve a low lasing threshold; (b) injection of high current density to reach the lasing threshold carrier density; (c) mitigating Joule heating under high current injection to reduce material degradation. These challenges have been partially resolved by a series of works. Room temperature continuous-wave lasing in quasi-2D perovskites has been achieved with second-order DFB gratings,[62] which showed the lasing threshold carrier density can be as low as 10^{16} cm^{-3}. DFB cavities can be well combined with LED structures to achieve ultrahigh current injection without material degradation. Zhao, et al. reported their LED structure with a second-order DFB cavity that achieved an electrical injection carrier density of 7.5×10^{17} cm^{-3} with 3D perovskites.[63] Although the room temperature continuous-wave lasing threshold carrier density (with quasi-2D perovskites) is already lower than the reported electrical injection carrier density (with 3D perovskites), laser diodes haven’t been achieved due to efficiency roll-off under high current injection.[47] Besides, quasi-2D perovskites with insulating spacers suffer more Joule heating than their 3D counterparts under high current injection, and they usually have a lower bimolecular recombination coefficient and higher Auger recombination coefficient.[39] Considering this, 3D perovskites with ultra-low quasi-CW pumped lasing threshold at room temperature pave a promising way to electrically pumped perovskite lasers. Recently, quasi-CW lasing from $MAPbBr_3$ at 260 K was achieved with a threshold of 4500 μJ cm^{-2}.[64]

As an important step towards electrically pumped lasers for integrated photonics, here we report an ultra-low lasing threshold quasi-CW pumped laser with $FAPbBr_3$ on first-order DFB cavities at room temperature. The ASE/lasing lifetime for perovskites is in the range of picoseconds, so the excitation with a pulse of longer duration can be considered as quasi-CW excitation.[30,58,64] Under 3.5 ns pulsed pumping, our device showed an ultra-low ASE threshold of 46 μJ cm^{-2}. The ASE threshold can be used as a benchmark for comparing different perovskites' intrinsic suitability for gain applications,[10] and our ASE thresholds are similar to the quasi-2D CW lasing devices,[62] A lasing linewidth of 0.6 nm was achieved with a lasing threshold of 22.6 μJ cm^{-2}, which is two orders of magnitude lower than a recent work on quasi-CW $MAPbBr_3$ laser.[64] The lasing peak can be tuned from 549.4 to 558.9 nm by changing the grating periods, as shown in Figure 21(b). The AFM images are shown in Figure 21(c)-(e), where second-order DFBs can be observed with a clear height contrast.

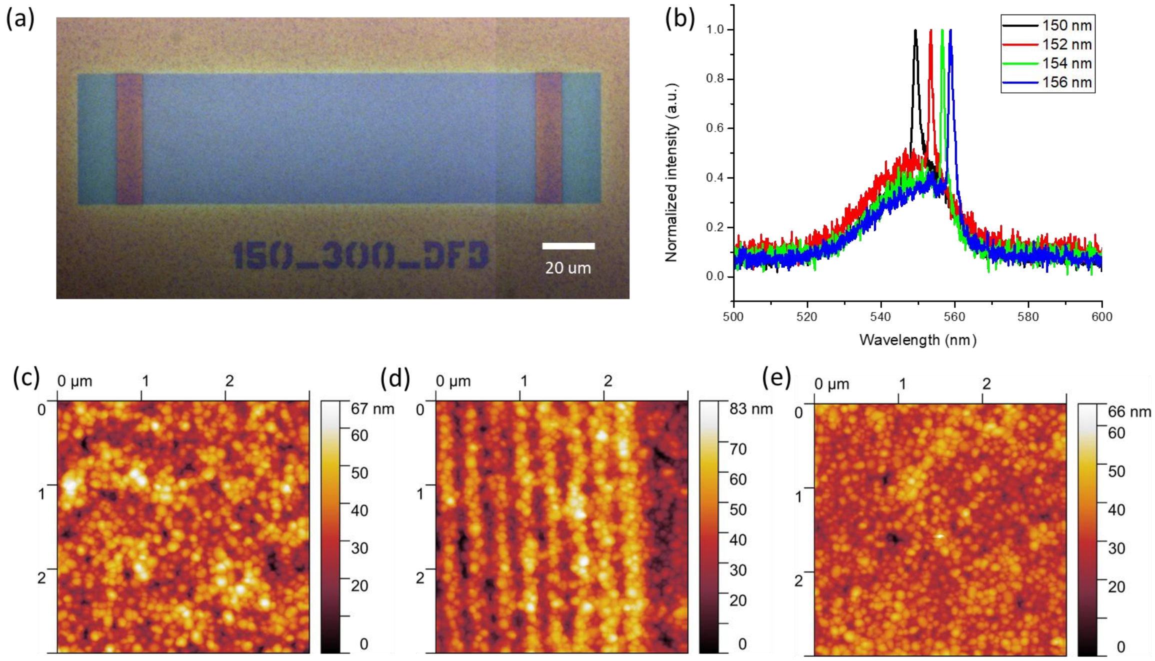

First-order DFB region
RMS: 9.54 nm

Second-order DFB region
RMS: 13.71 nm

Waveguide region
RMS: 6.42 nm

Figure 21 Laser design. (a) Perovskites on DFB cavities under the microscope. The image is spliced with two photos of the same grating. (b) Dependence of the lasing peak wavelength on the grating period of the first-order DFB gratings. (c)-(e) AFM images of the grating area.

For optically pumped lasers, the pumping source will make a difference in the devices' performances. Under ASE/lasing conditions, perovskites have a photon lifetime of 1-100 ps. When the pumping source has a shorter pulse than the photon lifetime, it should be considered pulsed pumping. Considering this, fs, ps and ns pump lasers will have different working mechanics during excitation. The lasing thresholds for some perovskite lasers' results with the same physical unit (energy/area/pulse width, in W/cm2) are listed in Table 3 for comparison.

Material	Pumping source	Threshold fluence	Threshold power density	Reference
$MAPbI_3$ thin film	150 fs, 1 kHz, 600 nm	ASE: 12 uJ cm^{-2}	8×10^{7} W cm^{-2}	[10]
$MAPbI_3$ nanowire	150 fs, 250 kHz, 402 nm	Lasing: 220 nJ cm^{-2}	1.47×10^{6} W cm^{-2}	[13]
$MAPbI_3$ nanoplate	50 fs, 1 kHz, 400 nm	Lasing: 37 uJ cm^{-2}	7.4×10^{8} W cm^{-2}	[11]

$FAPbBr_3$ micro-disk	100 fs, 1 kHz,	Lasing: 10-70 uJ cm^{-2}	1-7×10^{8} W cm^{-2}	[58]
P2F8/N2F8 thin film	Lasing: CW, 488 nm ASE: 3ns, 337 nm, 20 Hz	ASE: 16.7 uJ cm^{-2}	Lasing: 45 W cm^{-2} ASE: 5.6 ×10^{3} W cm^{-2}	[62]
$MAPbBr_3$	17 ns, 355 nm	Lasing: 4.5 mJ cm^{-2} ASE: 10 mJ cm^{-2}	Lasing: 2.6×10^{5} W cm^{-2} ASE: 5.9×10^{5} W cm^{-2}	[64]
$MAPbBr_3$	3.5ns, 337 nm, 20 Hz	Lasing: 60 uJ cm^{-2} ASE: 400 uJ cm^{-2}	Lasing: 1.7 ×10^{4} W cm^{-2} ASE: 1.1 ×10^{5} W cm^{-2}	[65]
$FAPbBr_3$	3.5ns, 337 nm, 20 Hz	Lasing: 22.6 uJ cm^{-2} ASE: 46 uJ cm^{-2}	Lasing: 6.4 ×10^{3} W cm^{-2} ASE: 1.3 ×10^{4} W cm^{-2}	This work

Table 3 A list of perovskite laser results.

4.3 ASE and lasing performance

For ASE and lasing measurement, a 3.5 ns pulsed laser (337 nm, 20 Hz repetition rate) was used as the pumping source. All measurements were done at room temperature with an ambient environment (around 22 °C, 60% humidity).

$FAPbBr_3$ shows an ultralow ASE threshold around 46 μJ cm^{-2}, which is about an order of magnitude lower compared with $MAPbBr_3$ in our previous work.[65] The ultralow ASE threshold proves the material to be excellent gain media for lasing applications. Figure 22(a) and (b) show the ASE's FWHM, output intensity and evolution of the ASE spectrum versus pump fluence. At low excitation, the spectrum shows a FWHM around 20 nm at 546 nm. At fluence above 46 μJ cm^{-2}, the FWHM drops to 2.8 nm and a sharp peak at 555 nm emerged, both indicating the onset of ASE.

A lasing threshold of 22.6 μJ cm^{-2} was achieved on the gratings with a period of 154 nm. The results presented in Figure 22(c) and (d) clearly indicate lasing of the perovskite laser. The emission spectrum shows a sharp peak with a FWHM of 0.6 nm once the pump fluence reaches the threshold. It is noted that the FWHM gradually increased with pump fluence. This is because the above lasing threshold linewidth is limited by and originates from coupled spontaneous emission noise.[66] In our case, the ASE threshold was very close to the lasing threshold and thus aggravated the effect.[23] Our pumping area is larger than the grating area, so some perovskites without gratings will also be excited and generate PL/ASE.

Interestingly, lasing cannot be observed from any second-order DFBs or photonic crystals on the same substrates. We would attribute this to the high outcoupling “loss” from these vertically outcoupling cavities, as well as the uneven surface with higher scatting loss. In low pumping regime, the outcoupled light is a loss to the cavity, overwhelming the optical gain and thus suppressing population inversion. In high pumping regime, the ASE dominates, and its spectrum overlaps with the lasing signal.[16]

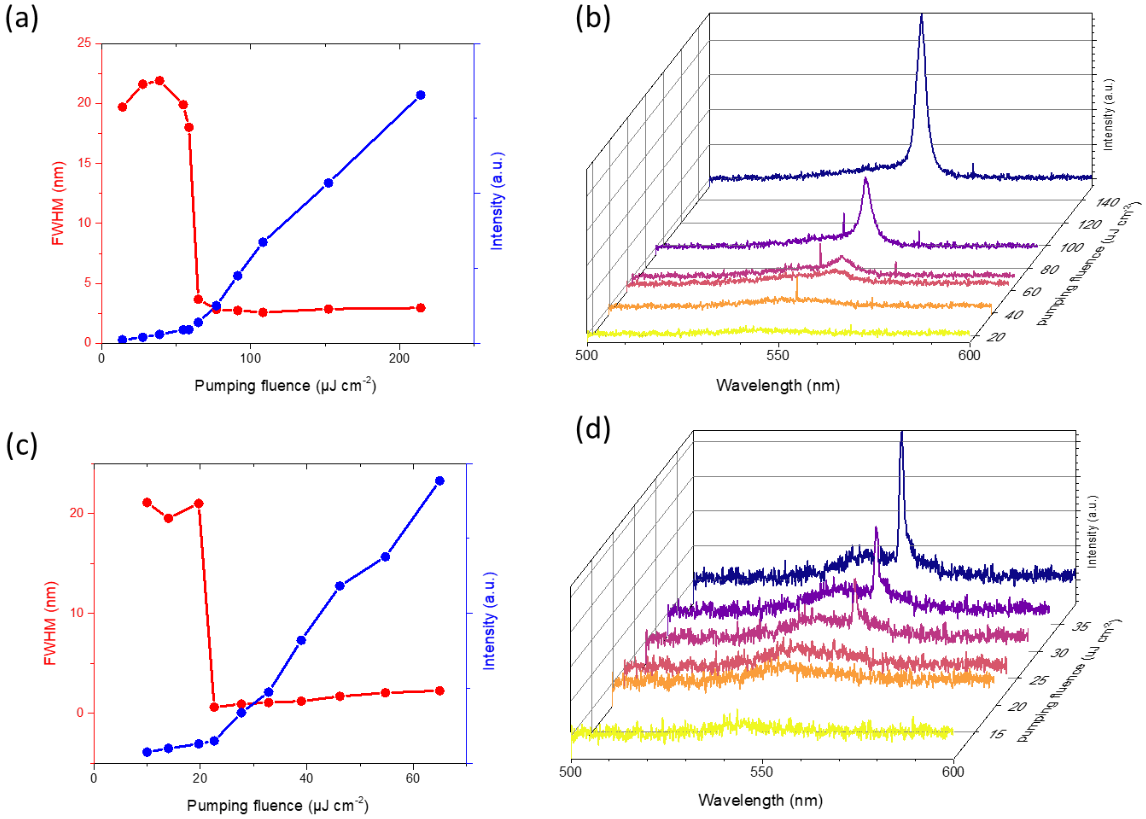

Figure 22 $FAPbBr_3$ laser's ASE and lasing performance. (a) FWHM and ASE intensity as a function of pump fluence. (b) Evolution of the ASE emission spectrum versus increasing pump fluence. (c) FWHM and laser output intensity as a function of pump fluence. (d) Evolution of lasing emission spectra under different pump fluences.

4.4 Polymer passivation

Using polymer additives is a common technique to passivate perovskites and thus improve perovskites' performance.[7,26,47] Here we used 18-crown-6 (crown) to passivate the perovskites and the results showed that this polymer can reduce ASE/lasing threshold and the crystal grain size.

In Figure 23(a), two devices with and without crown are compared. These two devices have exactly the same DFB designs and were deposited with perovskites together in the same fabrication round, to avoid any fabrication variance. Compared with the device without crown, the device with crown showed lower ASE (about 16% decrease) and lasing (about 15%, 29%, 26% and 26% decrease for 156 nm, 158 nm, another 158 nm and 160 nm gratings respectively) threshold.

To show the statistical significance of the crown passivation, a set of nominally identical devices was measured and the results are shown in Figure 23(b). Since the lasing thresholds for different grating periods are almost the same, they are all collected and shown here. The average ASE thresholds for devices without and with crown are 64.3 and 53.4 μJ cm^{-2}. The average lasing thresholds for devices without and with crown are 42.5 and 37.7 μJ cm^{-2}.

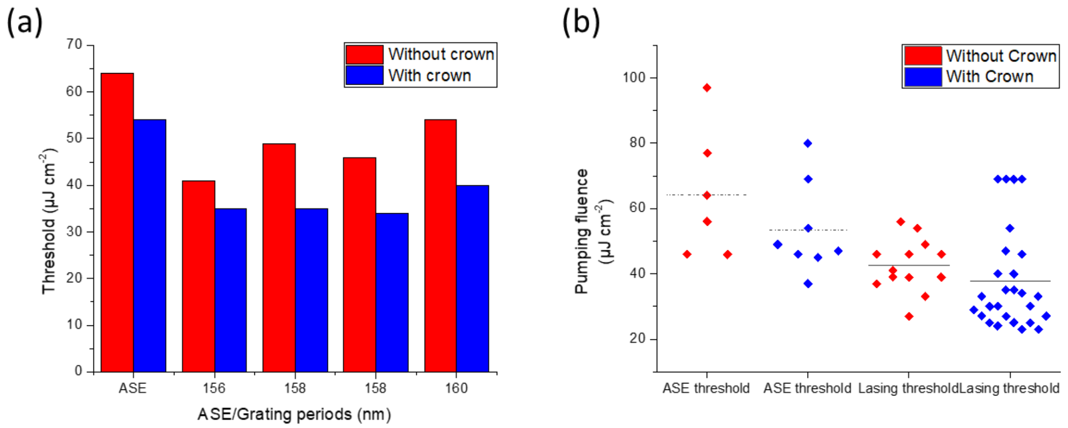

Figure 23 Statistic on polymer doping. (a) Comparison of ASE/lasing threshold between two samples with or without crown fabricated in the same round. (b) Statistics on ASE/lasing thresholds of a number of devices with or without crown. The average ASE thresholds for devices without and with crown are 64.3 and 53.4 μJ cm^{-2}. The average lasing thresholds for devices without and with crown are 42.5 and 37.7 μJ cm^{-2}.

With the addition of crown, the (100) orientation crystals have an increased ratio compared to (200), and the average crystal grain size is reduced. As XRD results shown in Figure 24, the chemical composition doesn't change with the addition of crown, but the crystal orientation and average crystal grain size are influenced. According to Scherrer equation:

$$\beta_{\frac{1}{2}}(2\theta) = \frac{K\lambda}{L\cos\theta}$$

Where $\beta_{1/2}$ is the FHWM of the peaks, θ is the peak position in degrees, K is a dimensionless shape factor, λ is the wavelength of radiation and L is the average crystal grain size. The calculated crystal grain sizes corresponding to each peak are listed in Table 4. A clear reduction in crystal grain size, especially in (100) orientation, is observed.

The reduction in grain size is also verified by SEM images shown in Figure 24(c) and (d). Both images are taken with a 50,000 magnification. The sample with crown shows much smaller crystal grains.

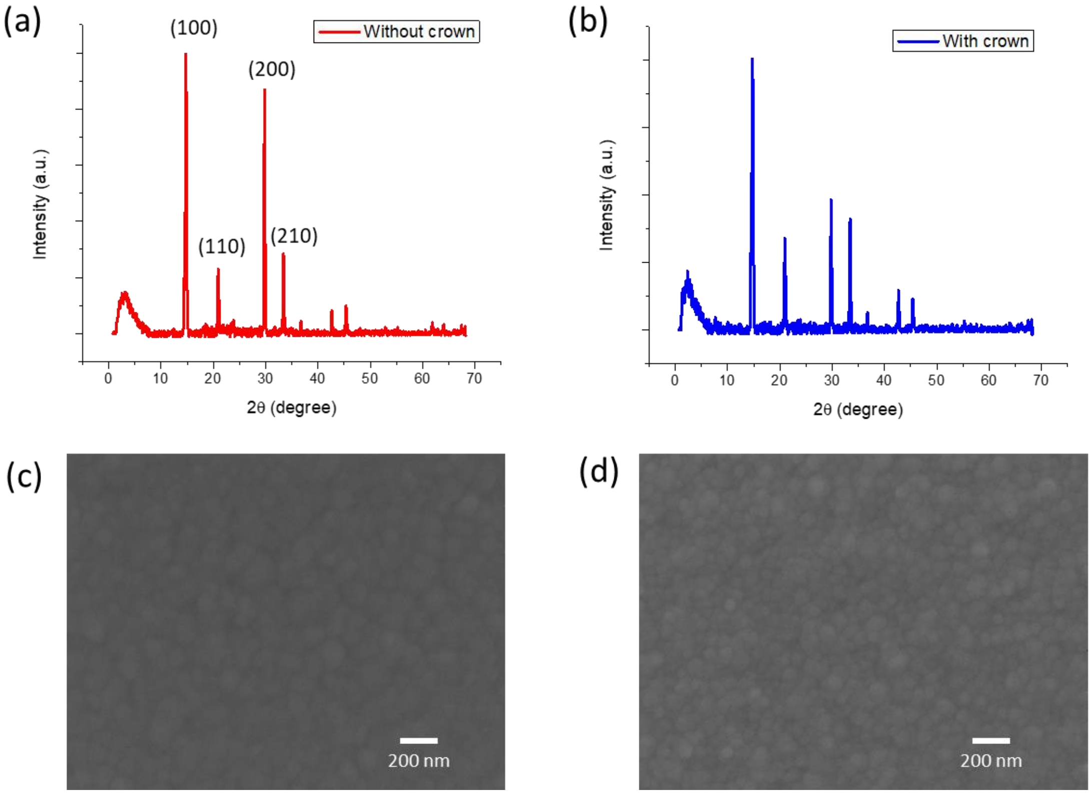

Figure 24 XRD and SEM results of FAPbBr3 samples before and after crown treatment. (a) and (b) are XRD results of the samples. After adding crown, the ratio of (100) crystal orientation increased and (200) decreased. (c) and (d) are SEM images of the sample without and with crown respectively. The sample with crown showed a smaller average grain size.

2θ (degree)	Average crystal grain size of $FAPbBr_3$ without crown (Å)	Average crystal grain size of $FAPbBr_3$ without crown (Å)
14	764.4	358.9
21	578.1	545.8
30	648.0	546.5
33	478.5	502.0

Table 4 The average crystal grain size of $FAPbBr_3$ before and after adding crown.

It is interesting to note that, the crown passivated devices showed a lower PL intensity and shorter PL lifetime. As is shown in Figure 25(a), the PL spectrum was measured under a 405 nm CW laser with a pump intensity of 420 mW/cm^2. The $FAPbBr_3$ film without crown showed a much higher peak at 545 nm, and TRPL result also showed it had a longer PL decay time (Table 5). The film with crown showed a clear biexponential decay with a fast decay term and slow decay term. The fast decay term is similar to previous results with $MAPbBr_3$ [65]. We also measured devices without PMMA encapsulation, as shown in Table 5. The addition of crown could extend the PL decay time by passivating the surface and reducing material degradation in the air.[26,37]

Counter-intuitively, samples with crown have a lower PL intensity, indicating a lower gain, at low pump fluence. However, they have a higher gain, thus a lower ASE/lasing threshold, at high pump fluence. This may seem a little contradictory when we compare the PL and ASE performance. The ASE threshold is determined by the injection carrier density when the waveguide gain exceeds the loss.[67] Consider carrier rate equation:

$$-\frac{dn(t)}{dt} = -G + k_1 n + k_2 n^2 + k_3 n^3$$

and the carrier lifetime:

$$\tau_{carrier} = \frac{1}{k_1 + k_2 n + k_3 n^2}$$

Where n is the charge carrier density, t is the time, k_1 is the monomolecular recombination rate (a trap-assisted Shockley-Read-Hall recombination), k_2 is the bimolecular recombination rate and k_3 is the Auger recombination rate, $\tau_{carrier}$ is the carrier lifetime.

PL intensity and PL lifetime are greatly influenced by trap density, or say the k_1 term. $FAPbBr_3$ with crown has a higher k_1 term compared to $FAPbBr_3$ without crown. The lower ASE threshold is attributed to the higher k_2 term. This result is consistent with observations in $MAPbI_3$ film, where k_2 increased from 1×10^{-10} cm^3s^{-1} to 2×10^{-9} cm^3s^{-1} after the grain size reduced from 170 nm to 20 nm.[38] The phenomenon could be explained by higher electron-hole pairs encountering possibility in the smaller gain area because the grain boundary restricts the diffusion of the charged carriers, leading to a higher k_2. The slightly higher k_1 can be understood by the increased defects on the grain boundary. To achieve a lower ASE/lasing threshold, a higher k_2 term and lower k_1, k_3 terms are favorable. k_1 term doesn't really influence the ASE/lasing behavior because ASE/lasing in 3D perovskites are mainly determined by free carriers in high pumping region where all traps are filled.[39]

From the carrier rate equation side, it's also easy to understand the lower ASE/lasing threshold behavior of $FAPbBr_3$ compared to $MAPbBr_3$. $FAPbBr_3$ has a much higher k_2 term and a lower k_3 term, as is shown in Table 6.

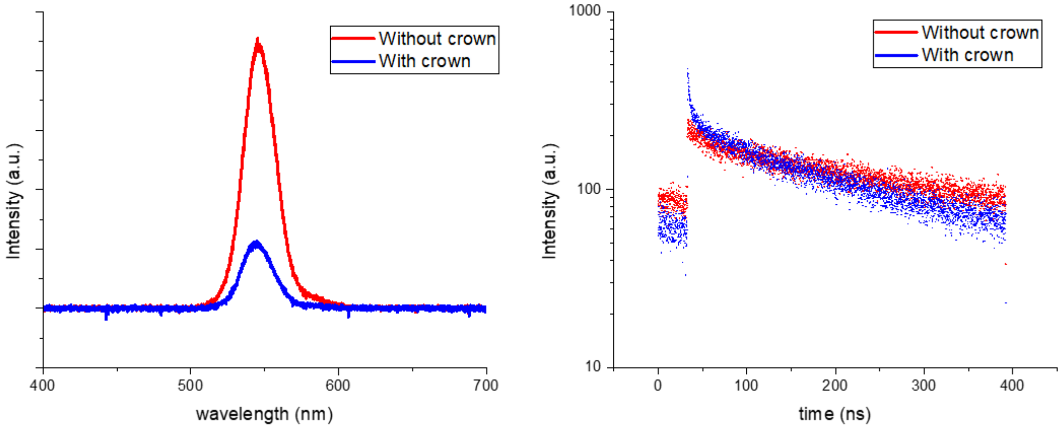

Figure 25 PL spectrum and PL lifetime of perovskites(a) PL spectrum for perovskite films without and with crown. (b) TRPL measurement for perovskite films without and with crown. The film with crown showed clear fast decay and slow decay terms.

	With PMMA encapsulation	Without PMMA encapsulation
Without crown	τ_1 = 263.9 ns, τ_2 = 16.4 ns	τ_1 = 9.9 ns, τ_2 = 9.9 ns
With crown	τ_1 = 192.7ns, τ_2 = 14.5 ns	τ_1 = 122.7 ns, τ_2 = 5.3 ns

Table 5 PL lifetime for films with/without PMMA and crown. With PMMA encapsulation, the sample with crown showed a faster PL decay compared to the sample without crown. When both samples were not encapsulated, the sample with crown shows a longer PL decay time due to better stability.

	K_1 (s^{-1})	k_2 (cm^3s^{-1})	K_3 (cm^6s^{-1})	*references*
$FAPbBr_3$	2.1×10^7	1.1×10^{-9}	1.5×10^{-28}	[68]
$MAPbBr_3$	2.7×10^7	4.9×10^{-10}	1.4×10^{-27}	[69]

Table 6 Recombination coefficients of $FAPbBr_3$ and $MAPbBr_3$.

4.5 Conclusion

In conclusion, we report an ultra-low lasing threshold quasi-CW pumped $FAPbbr_3$ laser at room temperature. The laser was fabricated with simple spin-coating and achieved orders of magnitude lower ASE/lasing threshold than recent $MAPbBr_3$ first-order DFB lasers.[64,65] With polymer additives, the performance of the material can be further improved, and we attribute the improvement to reduced grain size. The results could provide a better view of perovskite lasers working dynamics.

Chapter 5. Perovskite patterning

Adapted with permission from:

Zou, C., Chang, C., Sun, D., Böhringer, K.F. and Lin, L.Y. Photolithographic Patterning of Perovskite Thin Films for Multicolor Display Applications. *Nano Letters*, *20*(5), pp.3710-3717.

5.1 Abstract

Metal halide perovskites have emerged as attractive materials for light-emitting devices. Their external quantum efficiency (EQE) has made rapid progress and is comparable to state-of-the-art organic and quantum dot LEDs. The simple solution-processing preparation, facile bandgap tunability, and narrow emission linewidth of metal halide perovskites present an appealing opportunity to exploit their superior optoelectronic properties for multi-color display applications. Unfortunately, the fragile chemical and physical nature of perovskites has posed limitations on their further development, primarily due to challenges in fabrication. In this work, we developed a high-resolution, large-scale photolithographic method to pattern multicolor perovskite films. This approach utilizes a dry lift-off process, employing parylene as an intermediary layer that can be easily mechanically peeled off from various substrates. By applying this method, we successfully fabricated red and green perovskite pixels on a single substrate, which could be further integrated into 3-color displays, making color converters with a blue backlight.

5.2 Introduction

In recent decades, there has been a growing interest in patterning techniques for solution-processed luminescent materials. These techniques have garnered significant attention due to their wide range of potential applications in full-color displays, image sensors, and lasers.[70-73] The widespread adoption of high-resolution lithographic patterning methods, such as photolithography and electron-beam lithography, has played a significant role in advancing organic and quantum dot (QD) optoelectronics. These methods have facilitated the commercialization of various micro- and nano-scale devices, including televisions (TVs), cameras, and thin-film transistors (TFTs), based on organic and QD technologies.[74-77]

Significant progress has been made in the field of perovskite-based materials, particularly in solar cells and light-emitting devices. However, the focus of these studies has predominantly been on synthesis, photo-physics, and device engineering. Unfortunately, the application of photolithographic and E-beam lithographic patterning techniques to perovskite devices is still quite limited. This limitation arises from the incompatibility of perovskite materials with most solvents used in these processes, as they can cause dissolution or damage to the perovskite layers.[78] Furthermore, the range of perovskite materials that can be successfully patterned using existing techniques is often limited. Consequently, this restricts the full potential of perovskite LEDs for display applications,[79] and the demonstration of lithographically patterned perovskite micro-LED arrays remains elusive.

In this study, we present a novel and versatile approach to pattern perovskite materials using photolithography at a micrometer resolution. This technique utilizes a dry lift-off process, eliminating the direct contact of solvents that can cause perovskite dissolution issues in common polar solvents. Throughout the fabrication process, the excellent optoelectronic properties of perovskite materials are preserved. Using this method, we successfully fabricate single-color perovskite patterns in red, green, and blue (RGB) with a minimum resolution of 4 um. Furthermore, we demonstrate the simultaneous fabrication of multicolor perovskite patterns emitting green and red light on a single substrate. With commercial blue backlight substrate (GaN), full-color displays can be achieved. Importantly, we achieve a significant milestone by successfully realizing perovskite micro-LED displays using this innovative patterning technique, which, to the best of our knowledge, has not been previously demonstrated.

5.3 Patterning fabrication process

Here, we report a new method utilizing parylene-C and a dry lift-off process [80]. This method demonstrates compatibility not only with perovskite materials but also with quantum dots, 2D materials, quasi-2D materials, and 3D perovskites, as shown in Figure 27(d). During the fabrication process, the perovskite materials are effectively isolated from the solvent, ensuring that their properties and performance remain unaffected. After the first perovskite layer is patterned, parylene can be deposited on top of it as a protection layer. Then, by repeating the process, different perovskite materials can be patterned on the same substrate. To showcase the effectiveness of our approach, we successfully patterned a dual-color perovskite pixel array. This demonstrates the utility and versatility of our method in creating intricate patterns with different colors in perovskite materials. Furthermore, our approach can be extended to the fabrication of perovskite micro-LED arrays, offering potential applications in high-resolution displays and optoelectronic devices.

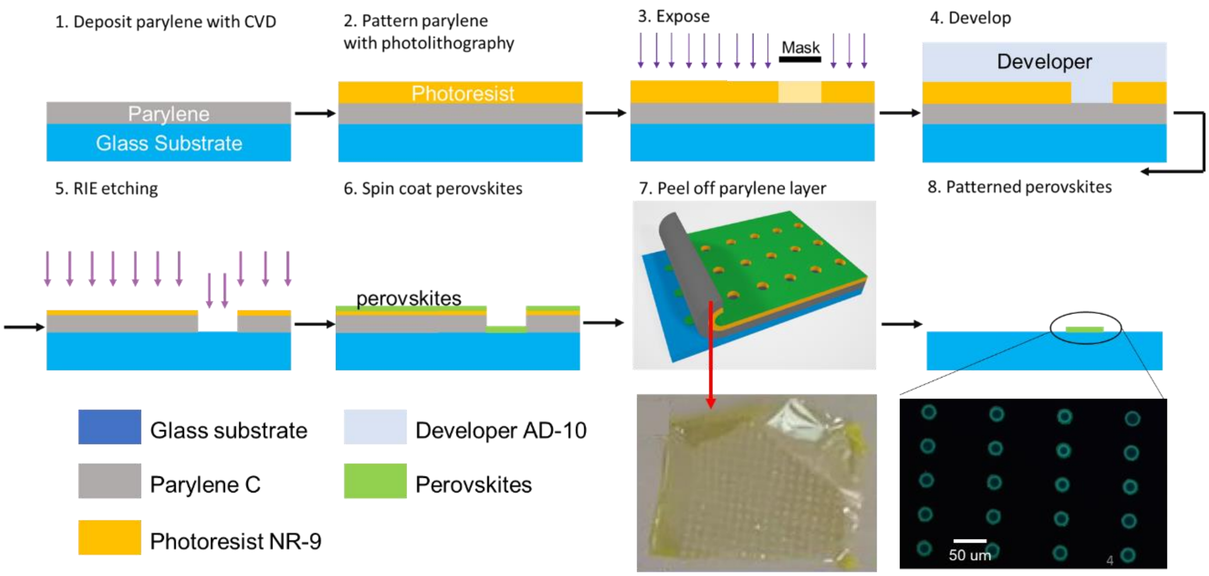

Figure 26 The fabrication process of the proposed method to achieve high-resolution patterning of perovskites. The process utilizes patterning parylene-C which is lifted off later to achieve perovskite patterns, avoiding any solvents contacting the perovskite layer.

The fabrication process of the proposed method is shown in Figure 26. A layer of 3 um parylene-C is first deposited on the substrate by chemical vapor deposition (CVD). A glass substrate is used as an example in our proof-of-concept demonstration. But this method is also compatible with other substrates. In later works, we used GaN wafers to get blue backlight. Photolithography is used to pattern the parylene-C. Negative photoresist is used for the illustration as shown in Step 2-4. Afterward, the parylene-C layer is etched through to the glass substrate. A thin layer (30 nm) of perovskite is spun cast on the surface. Since parylene-C is hydrophobic with high structural integrity and strength, it’s easy to peel off the entire layer through mechanical means, as illustrated in Step 7. During this lift-off process, the perovskite layer does not come into contact with any chemicals or solvents, so its electrical and optical properties will be well preserved. Using this approach, we could pattern large-scale and multicolor perovskite films on various substrates with a minimum resolution of 4 μm (step 8 shows the circle patterns of the perovskites).

To guarantee a good fabrication result with parylene lift-off, a series of steps need to be carefully handled:

(1) The thickness of the parylene layer involves a trade-off in the fabrication process. Thicker parylene layers facilitate easier lift-off but may result in lower pattern resolution due to undercutting or overcutting during etching (as shown in Figure 27(a)). An effective approach to improving pattern resolution is to utilize a metal mask instead of a resist mask.

(2) A ring can be seen in perovskite patterns, which is resulted from the spin coating. During spin coating, perovskites are spun cast on the sidewall of parylene, forming a thicker edge after lift-off (Figure 27(a)). By evaporation, perovskite patterns will have a much smoother profile (Figure 27(d)).

(3) Lift-off using parylene can be challenging (Figure 27(b)-(c)). The success of the process relies on achieving a smooth surface on the underlying substrate. Applying a spin coating of micro-90, which is a cleaning detergent for parylene, can reduce adhesion and facilitate the lift-off process.

(4) Parylene becomes hardened and challenging to peel off above 150 ℃. It is crucial to use lower temperatures during perovskite annealing, resist annealing, and metal evaporation to prevent adverse effects on the parylene layer.

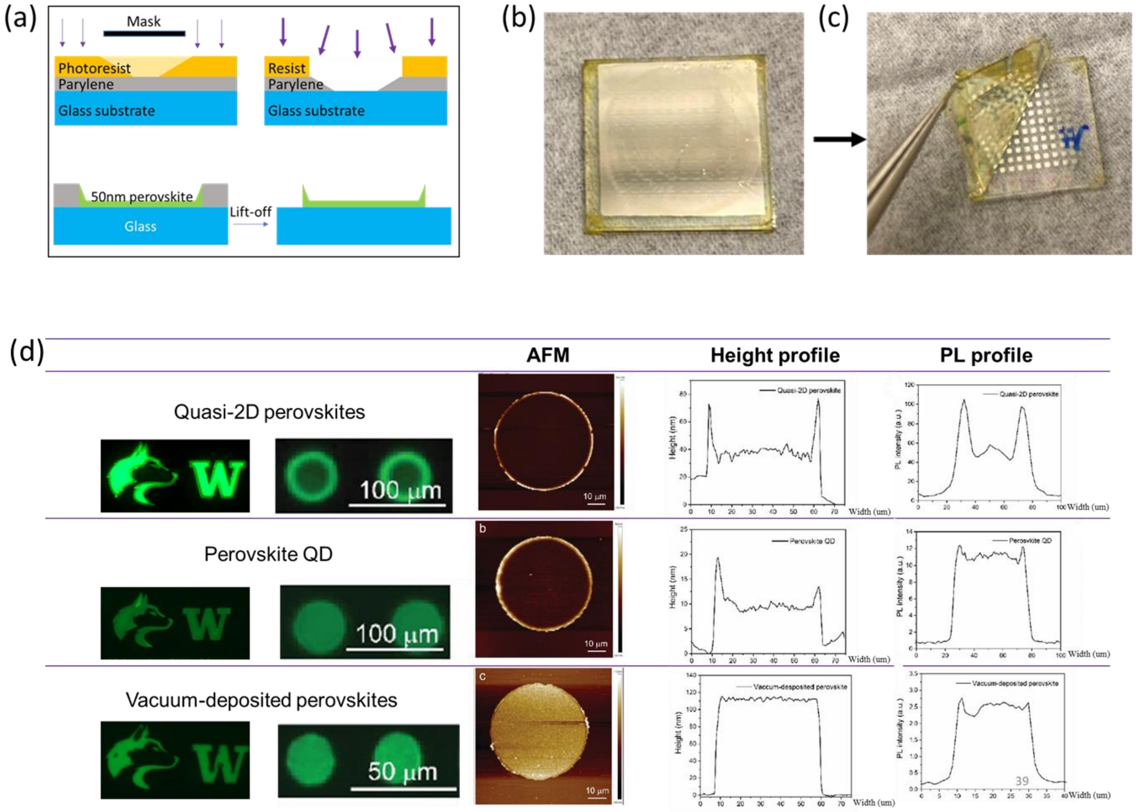

Figure 27 Perovskite patterning. (a) Common fabrication issues with parylene. (b) and (c) lifting off parylene with a tweezer. The patterned pixel (perovskites with silver) can be seen. (d) Different types of perovskites' patterning results. The major difference is that quasi-2d and QD perovskites have a ring-like edge. The vacuum-deposited perovskites show a much smoother and more uniform profile. This is because both quasi-2d and QD are deposited by spin coating, the centripetal force makes perovskites accumulate at the edge.

5.4 Results and discussion

5.4.1 Single-color patterns

Figure 28 presents optical images of RGB-emitting perovskite films under UV excitation, showcasing their strong photoluminescence (PL). Blue, green and red perovskite circles (50 μm diameter) are shown in Figure 28(a)-(c). In addition, the University of Washington logos emitting blue, green and red lights are displayed in Figure 28(d)-(f). The blue and green perovskite patterns exhibit strong luminescence with high color contrast. However, the red perovskite pattern shows relatively lower contrast due to the environmental instability of red perovskites. Figure 28(g) shows blue, green and red perovskite emission spectra. The peak wavelength is 482, 523 and 670 nm for blue, green and red-emission perovskite thin films, respectively. The green perovskite films show the narrowest linewidth of ~17 nm while the linewidth is ~28 and ~38 nm for blue and red perovskite films, respectively.

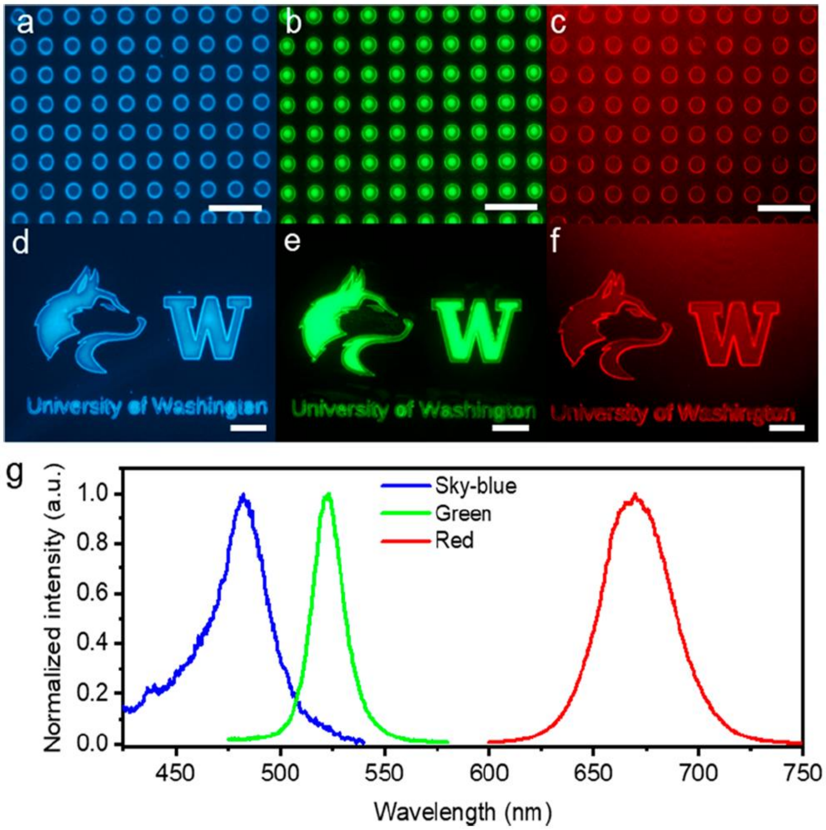

Figure 28 Single-color perovskite patterns. (a)-(c) Blue, green and red perovskite circles (50 μm diameter). (d)-(f) University of Washington logos, scale bar 200 μm. (g) PL spectra of blue, green and red perovskite films.

5.4.2 Multi-color patterns

To achieve commercial RGB displays, a common approach is to fabricate green and red pixels together on a single substrate with blue backlights underneath, which is widely used in LCD applications.[71,77] The green and red-emitting pixels can absorb blue light and convert it into green and red light, enabling the realization of true RGB displays. In this study, we utilize standard photolithography combined with the demonstrated dry lift-off process twice to sequentially pattern green and red perovskite on the same glass substrate. Figure 29(a) schematically illustrates the fabrication procedures. Parylene and photoresist are sequentially deposited onto the substrate with pre-fabricated green perovskite patterns. Figure 29(b) displays the uniform array of alternative green and red perovskite circles, each circle has a diameter of ~50 μm. The magnified fluorescent image is shown in Figure 29(c), the second photolithography and lift-off processes didn't affect the pre-fabricated green perovskite patterns due to the excellent sealing of parylene films. The perovskite films covered by parylene can even survive in acetone solution for several days. We also measured the overall PL spectrum contributed by both green and red perovskite circles at the same time (Figure 29(d)). The overall PL from multicolor patterns shows two emission peaks located separately at the green and red wavelength regions. The peak PL intensity of green perovskite patterns is about 2.5-fold as high as that of red ones. This difference can be easily understood considering the relatively poor PLQY and stability of red-emission perovskites which include more iodine halides. Figure 29(e) shows the PL spectra of green perovskite patterns before and after the second patterning process. There is only a slight drop in PL intensity observed after the second patterning process which includes many steps such as resist deposition, UV exposure, development, RIE and lift-off. This indicates our approach preserves the properties of pre-fabricated perovskite patterns and multiple patterning processes are feasible.

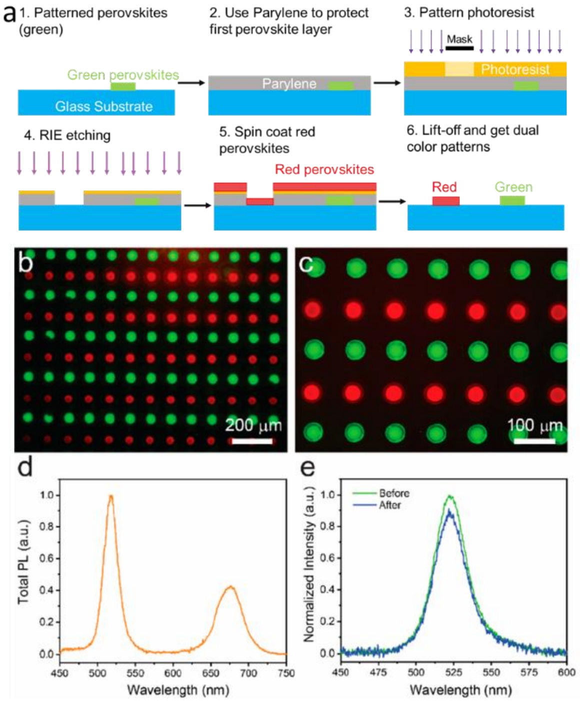

Figure 29 Multi-color perovskite patterning. (a) The schematic fabrication procedures of multi-color perovskite patterns. (b) Fluorescent microscope image of green and red perovskite circles with a diameter of 50 μm. (c) Higher magnification fluorescent image of the dual-color patterns. (d) Overall PL spectrum of the dual-color perovskite patterns. (e) PL spectra comparison of green perovskite patterns before and after the second patterning process.

5.4.3 Perovskite color converters

Based on the patterning techniques for perovskite materials, it is possible to develop perovskite color converters. These converters are commonly used to enhance the color quality and efficiency of light-emitting diodes. LED devices often have limitations in color quality as they emit light within a narrow range of wavelengths or colors. By integrating perovskite layers into a blue GaN LED wafer (Figure 30(a)), it becomes feasible to modify the emitted light's color. The perovskite material absorbs a portion of the original light and re-emits it at a different wavelength, resulting in a broader spectrum of colors. This process, known as down-conversion, shifts the light to longer wavelengths.

Perovskite color converters offer several advantages, including tunability, high color purity, and potentially high conversion efficiencies. Perovskite materials can be precisely engineered to possess specific absorption and emission characteristics, enabling precise control over the resulting color output. Additionally, as a passive layer, the perovskite converter's lifetime can be significantly improved compared to perovskite LEDs. The degradation pathways that affect perovskite LEDs, such as ion migration under electrical fields and Joule heating, do not influence perovskite converting layers.

The device structure is depicted in Figure 30(a). The GaN LED wafer is purchased from UniversityWafer and then processed in WNF. The emitting wavelength for these LEDs is around 450 nm. We used our green PQDs as the conversion layer since (1) our PQDs have the highest PLQY compared with 3D and quasi-2D perovskites. (2) PQDs are intrinsically encapsulated by organic ligands and thus to be super stable in the air.

The working device is shown in Figure 30(c), where a greenish pixel is visible within the blue LED. Figure 30(d)&(e) shows the perovskite patterns in bright field (backlight off) and dark field (backlight on), respectively, with a distinct green pattern observable. It should be noted that the edges of the patterns appear brighter due to variations in film thickness.

In solution (Figure 6(c)), PQDs exhibit a PLQY of over 99.6%, which can be regarded as close to unity. However, when spin-coated as films, the PLQY of PQDs decreases due to film defects and scattering losses. An energy distribution diagram for the perovskite color converter device is shown in Figure 30(b). The absorption of perovskite conversion layer is determined by:

$$A = I_0(1 - e^{-\alpha d})$$

Where A is absorption, I_o is the excitation, α is absorption coefficient and d is the film thickness. Our device has overall 49.9% PLQY and 11.7% conversion efficiency.

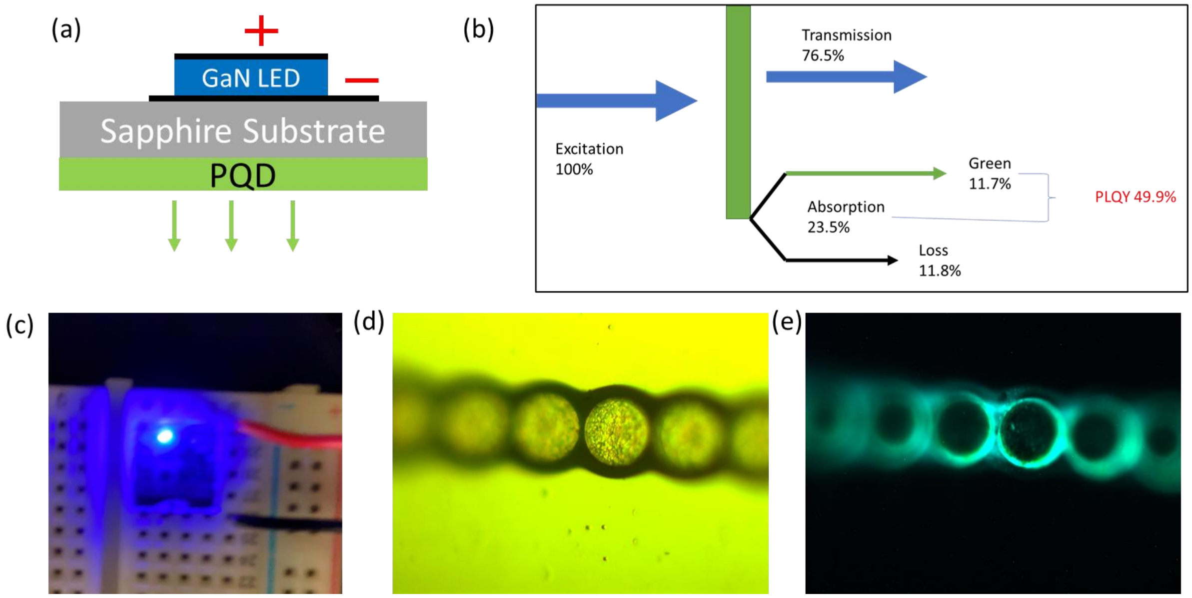

Figure 30 Perovskite color converter. (a) Perovskite color converter with GaN LED as backlight. (b) Energy distribution diagram for the perovskite color converter. (c) A working perovskite color converter device. (d)&(e) Perovskite patterns in bright field (backlight off) and dark field (backlight on).

The idea of increasing conversion efficiency by increasing the thickness of the perovskite film seems intuitive. According to calculations, a few-hundred nanometer film should efficiently absorb around 99% of the blue excitation light. However, we encountered limitations due to the low concentration of our PQD solution. When drop-casting, the resulting PQD film thickness was only around 10 nm, significantly thinner than expected. We attempted multiple drop-casting steps to form thicker films, but the total conversion efficiency did not improve.

Figure 31 (a) presents the PLQY, absorption, and conversion efficiency values for films produced through 1-5 drop-casting steps. It is evident that as the number of drop casts increases, there is a clear rise in absorption and a decrease in PLQY. The decline in PLQY can be attributed to the formation of a rough and uneven surface after multiple drop casts, which is apparent in Figure 31 (b)&(c).

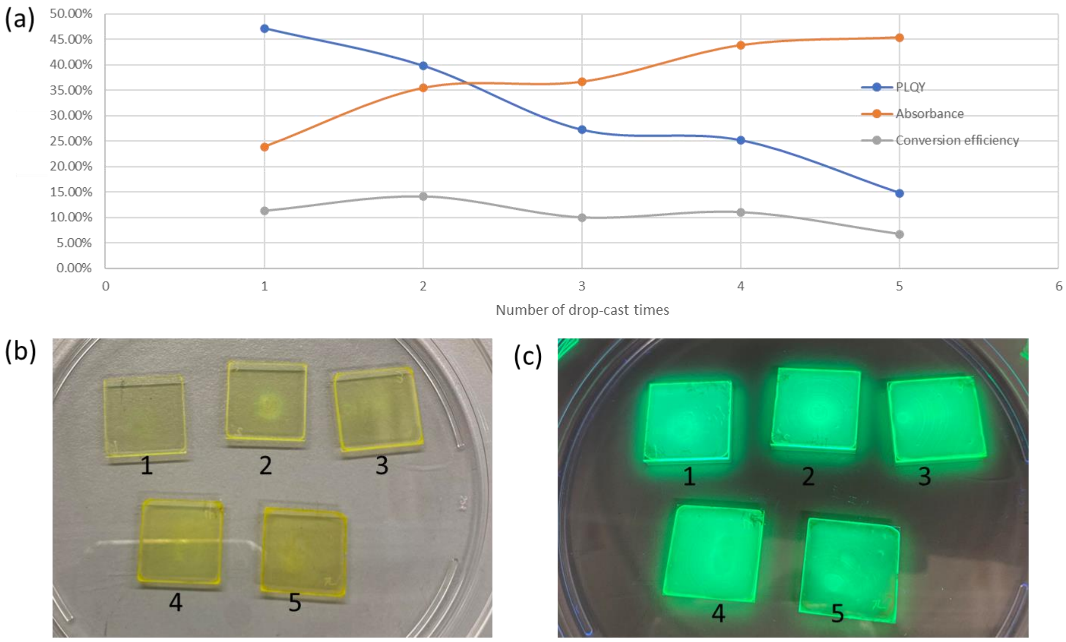

Figure 31 Multi drop cast perovskite films. (a) The PLQY, absorption, and conversion efficiency values for films produced through 1-5 drop-casting steps. (b)&(c) Perovskite films produced through 1-5 drop-casting steps under light and UV light.

5.4.4 Perovskite micro-LEDs

Micro-LED utilizes tiny light-emitting diodes as individual pixels to create a display panel. These LEDs are typically smaller in size compared to traditional LEDs, often ranging from 10 to 100 micrometers in length, hence the term "micro-LED." Micro-LED displays are being actively researched and developed for various applications, including consumer electronics, signage, automotive displays, and wearable devices.

Here, we combined the novel dry lift-off process involving traditional photolithography to build a perovskite micro-LED array.[80] During the process, the perovskite layer is not exposed to any solvents for photolithography, therefore the process is compatible with all kinds of perovskite materials. Each pixel in the array is controlled individually by a cross-link electrode matrix. With further optimization and integration, an all-color perovskite micro-LED display with high resolution can be achieved.

The fabrication workflow of the perovskite LED array is shown in Figure 32. First, a layer of indium tin oxide (ITO) is deposited on the substrate in a desired pattern as bottom electrodes. Due to the fact that perovskites dissolve in most polar solvents including photolithographic developers, an intermediary layer of parylene-C is used to pattern and protect the perovskites. This intermediary layer is first etched with patterns by photolithography (Figure 32(b)). Then, hole transporting layer (HTL)/perovskite layer/electron transporting layer (ETL) are deposited on top of the intermediary layer in sequence (Figure 32(c)). After that, the intermediary layer is lifted off mechanically, leaving the patterned perovskite LED pixels on the bottom electrodes as shown in Figure 32(d). Since perovskite LED pixels are still vulnerable during the fabrication, another intermediary layer is used to cover the perovskites and then patterned as shown in Figure 32(e). The top electrodes are deposited and patterned through the same process as described above. With careful alignment, the top and bottom electrodes can cross-link all the perovskite LED pixels and form a display array with individually addressable pixels (Figure 32(f)).

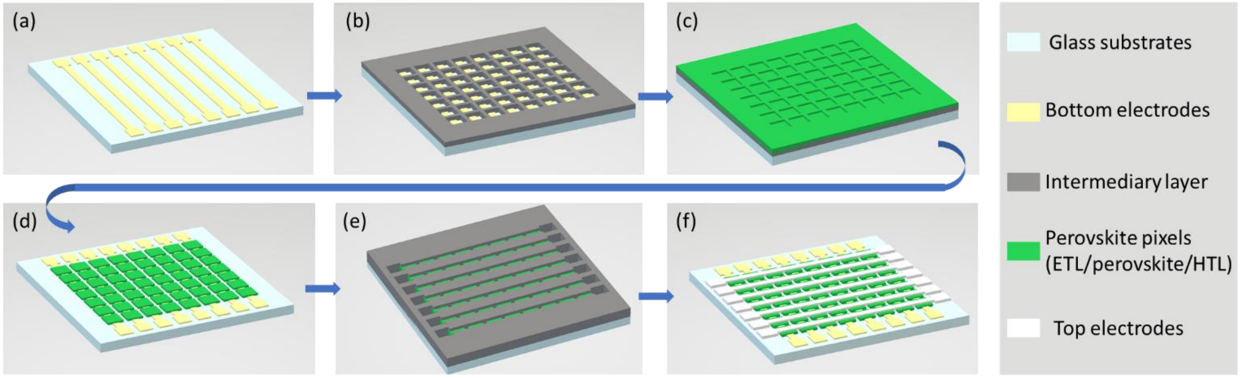

Figure 32. Fabrication process of the perovskite LED array. (a) Deposit patterned bottom electrodes on the substrate. (b) Pattern an intermediary layer of parylene-C on top of the electrode. (c) Spin-coat emission layers (HTL/perovskites/ETL) on the intermediary layer. (d) Lift off the intermediary layer and patterned pixels are formed. (e) Deposit and pattern another intermediary layer for the top electrode patterns. (f) Deposit the top electrode and lift off the intermediary layer.

The whole device (in Figure 33(a)) is fabricated on a 15 mm × 15 mm glass substrate. There are 100 pixels controlled by 10 top electrodes (in column) and 10 bottom electrodes (in row) individually. The top and bottom electrodes are 200 μm in width, which define the working pixels each with an area of 200 um×200 um, as shown in Figure 33(b). Figure 33(c) shows a single perovskite LED pixel turned on by applying the 8th top electrode column and 10th bottom electrode row with bias. By sweeping the on/off state of each electrode with a desired frequency, all the pixels can be turned on and off in certain sequence. An external circuit can be incorporated to selectively address multiple pixels simultaneously. By repeating the dry lift-off lithography process in Figure 32(c) and (d), different perovskite materials emitting different colors can be integrated, forming a full-color display.

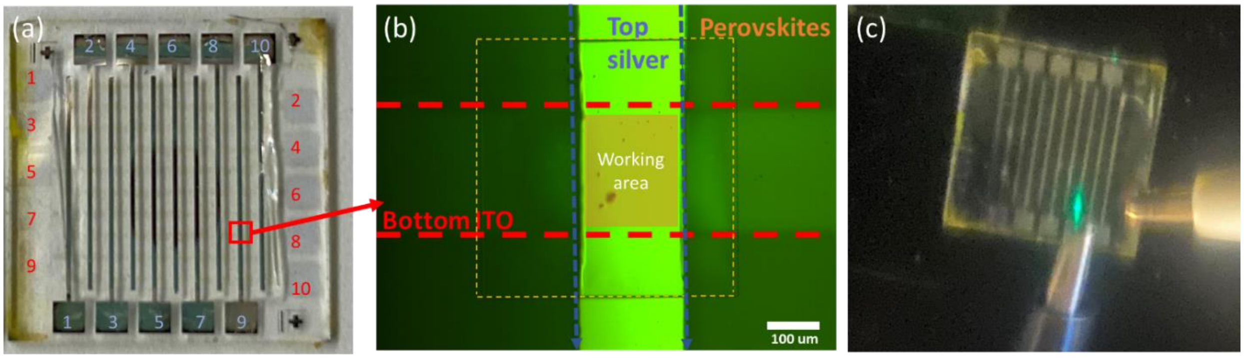

Figure 33. Perovskite micro-LEDs. (a) Fabricated device. The red square indicates the area for a single pixel. (b) A single pixel under microscope. The red and blue dash lines indicate the bottom and top electrodes. The dashed orange area is a perovskites pixel. (c) A single pixel working under an applied bias.

5.5 Conclusion

In conclusion, our study presents a dry lift-off fabrication method that enables precise patterning of perovskite materials. This method allows for high-resolution and multi-color perovskite patterns to be achieved. Importantly, the excellent quality of the perovskite materials is preserved throughout the fabrication process. With further optimization, the method holds potential for improving fabrication outcomes. Additionally, beyond simple patterns, more complex devices such as micro-LED arrays and photodetectors can be feasibly fabricated using a this process and will be demonstrated in following chapters.

Chapter 6. Conclusion and prospects

6.1 Summary

Metal halide perovskites have gained significant attention due to their exceptional optoelectronic properties, making them promising candidates for various applications including solar cells, LEDs, and lasers. In this dissertation, my focus is specifically on the lasing applications of perovskites. These materials exhibit high PLQY, efficient charge transport, tunable emission wavelengths, narrow emission linewidth, and low fabrication cost, making them highly attractive for solution-processed lasers.

The progress in perovskite light-emitting diodes (PeLEDs) has been remarkable over the past decade. Numerous research groups have achieved significant improvements in the external quantum efficiency (EQE) of PeLEDs, with values increasing from as low as 0.1% to over 28%. This remarkable enhancement in EQE demonstrates the potential of perovskite materials for high-performance light-emitting devices. Moreover, the near-unity photoluminescence quantum yield (PLQY) of perovskite materials opens up possibilities for integrating perovskite color converters into traditional LEDs. By incorporating perovskite color converters, the color quality and efficiency of LEDs can be significantly improved, leading to the fabrication of high-performance displays. This approach allows for precise control over the emitted colors and enables the production of vibrant and accurate displays. Furthermore, the development of perovskite lasers has generated excitement and hope for the realization of electrically pumped laser diodes based on perovskite materials. The unique properties of perovskites, such as their high PLQY and excellent charge transport, make them promising candidates for electrically driven lasers. The progress in perovskite laser research brings the potential for compact and efficient electrically pumped lasers, which could have significant implications in various applications, including optical communication, sensing, and display technologies. All these achievements emphasize the potential of perovskites as a reliable platform for efficient and scalable light-emitting devices.

Chapter 1 and Chapter 2 provided a comprehensive overview of perovskite materials for lasing applications. We talked about their chemical properties, optoelectronic properties, applications and synthesis methods, which are fundamental to my research.

In Chapter 3 and Chapter 4, we focused on the development of optically pumped perovskite lasers. We conducted a comprehensive investigation into the design, fabrication, and optimization of 1st-order distributed feedback (DFB) lasers using two different perovskite materials: $MAPbBr_3$ and $FAPbBr_3$. For MAPbBr3, the lasing threshold was measured to be 60 μJ cm^{-2} under nanosecond pumping, while for FAPbBr3, it was even lower at 22 μJ cm^{-2}. Notably, the threshold for amplified spontaneous emission (ASE) in $FAPbBr_3$ was one order of magnitude lower than that of $MAPbBr_3$. To further enhance the performance and stability of the lasers, we explored various methods and discussed their results in detail. Firstly, we found that the use of 1st-order DFB lasers resulted in a 60% reduction in lasing threshold compared to 2nd-order DFB lasers, indicating the effectiveness of the design approach. Additionally, we investigated the impact of anti-solvent treatments on film quality and laser performance. Through the application of thin PMMA layer encapsulation, we observed significant improvements in laser performance and stability. Furthermore, the introduction of polymer additives showed promising results in enhancing the performance of the perovskite material. This improvement was attributed to the reduction in grain size, which positively influenced the overall laser performance. Our findings not only provide valuable insights into the working dynamics of perovskite lasers but also offer potential strategies for reducing lasing thresholds and improving device stability. These advancements in optically pumped perovskite lasers hold great significance for the development of efficient and reliable light sources for various applications in the field of photonics and beyond.

In Chapter 5, we have successfully developed a high-resolution dry lift-off photolithographic method for patterning perovskite films, specifically targeting their application in displays. Metal halide perovskites offer a compelling opportunity for multi-color display applications due to their simple solution-processing preparation, facile bandgap tunability, and narrow emission linewidth. However, the fragility of perovskite materials has hindered their progress, particularly in terms of fabrication techniques. To address this challenge, we have developed a dry lift-off process that incorporates an intermediary layer of parylene. This parylene layer acts as a protective barrier and can be easily mechanically peeled off from various substrates. By implementing our method, we have successfully manufactured red and green perovskite pixels on a single substrate. These pixels can be further integrated into three-color displays, allowing them to function as color converters when combined with a blue backlight.

6.2 Future work outlook

As an emerging candidate in the field of solution-processed emitters, perovskites have demonstrated remarkable optoelectronic properties that surpass those of previous leading contenders such as organic semiconductors and colloidal nanocrystals. The ongoing development of perovskite light-emitting devices holds significant interest and importance for the advancement of next-generation display and laser applications.

The next major step for perovskite light-emitting devices is the commercialization of PeLEDs and the realization of perovskite laser diodes. However, both of these goals require improvements in the stability of perovskites under current injection. Ensuring long-term device performance and reliability is crucial for their practical implementation.

While optically pumped perovskite lasers and LEDs have seen significant development, electrically pumped perovskite lasers remain a long-standing challenge in laser research. However, the successful demonstration of organic polymer lasers has provided a possible direction for achieving electrically pumped perovskite lasers. Recent advancements have shown that the lasing threshold of pulsed optically pumped perovskite lasers can reach as low as 0.2 μJ cm^{-2}, and room-temperature continuous-wave lasing has been realized, indicating the great promise of perovskites in the field of lasers.

To achieve perovskite lasers with LED structures, several primary challenges need to be addressed. First, it is necessary to incorporate perovskites into a high-quality optical feedback structure with high gain to enable lasing. Second, the injection of high current density is required to reach the lasing thresholds, which poses challenges in terms of charge transport and device design. Third, effective strategies must be developed to mitigate Joule heating under high current injection and reduce material degradation, ensuring long-term device stability. Finally, efforts should be made to reduce photon quenching induced by metal electrodes and the electric field to enhance the overall device performance.

By addressing these challenges and advancing the understanding of perovskite materials and devices, we can pave the way for the commercialization of perovskite light-emitting devices and the realization of electrically pumped perovskite lasers. These advancements have the potential to revolutionize the field of optoelectronics and open up new possibilities for next-generation display and laser technologies.

Reference

1 Jena, A. K., Kulkarni, A. & Miyasaka, T. Halide Perovskite Photovoltaics: Background, Status, and Future Prospects. *Chem Rev* **119**, 3036-3103, doi:10.1021/acs.chemrev.8b00539 (2019).

2 Green, M. A., Jiang, Y., Soufiani, A. M. & Ho-Baillie, A. Optical Properties of Photovoltaic Organic-Inorganic Lead Halide Perovskites. *J Phys Chem Lett* **6**, 4774-4785, doi:10.1021/acs.jpclett.5b01865 (2015).

3 Green, M. A., Ho-Baillie, A. & Snaith, H. J. The emergence of perovskite solar cells. *Nature Photonics* **8**, 506-514, doi:10.1038/nphoton.2014.134 (2014).

4 Dong, H. *et al.* Metal Halide Perovskite for next-generation optoelectronics: progresses and prospects. *eLight* **3**, doi:10.1186/s43593-022-00033-z (2023).

5 Min, H. *et al.* Perovskite solar cells with atomically coherent interlayers on SnO2 electrodes. *Nature* **598**, 444-450 (2021).

6 Shen, Y. *et al.* High‐efficiency perovskite light‐emitting diodes with synergetic outcoupling enhancement. *Advanced Materials* **31**, 1901517 (2019).

7 Liu, Z. *et al.* Perovskite Light-Emitting Diodes with EQE Exceeding 28% through a Synergetic Dual-Additive Strategy for Defect Passivation and Nanostructure Regulation. *Adv Mater* **33**, e2103268, doi:10.1002/adma.202103268 (2021).

8 Kondo, T., Azuma, T., Yuasa, T. & Ito, R. Biexciton lasing in the layered perovskite-type material (C6H13NH3)2PbI4. *Solid State Communications* **105**, 253-255, doi:10.1016/s0038-1098(97)10085-0 (1998).

9 Kondo, S., Suzuki, K., Saito, T., Asada, H. & Nakagawa, H. Photoluminescence and stimulated emission from microcrystalline<mml:math xmlns:mml="http://www.w3.org/1998/Math/MathML" display="inline"><mml:mrow><mml:mi mathvariant="normal">Cs</mml:mi><mml:mi mathvariant="normal">Pb</mml:mi><mml:msub><mml:mi mathvarian. *Physical Review B* **70**, doi:10.1103/physrevb.70.205322 (2004).

10 Xing, G. *et al.* Low-temperature solution-processed wavelength-tunable perovskites for lasing. *Nature Materials* **13**, 476-480, doi:10.1038/nmat3911 (2014).

11 Zhang, Q., Ha, S. T., Liu, X., Sum, T. C. & Xiong, Q. Room-Temperature Near-Infrared High-Q Perovskite Whispering-Gallery Planar Nanolasers. *Nano Letters* **14**, 5995-6001, doi:10.1021/nl503057g (2014).

12 Tan, Z.-K. *et al.* Bright light-emitting diodes based on organometal halide perovskite. *Nature Nanotechnology* **9**, 687-692, doi:10.1038/nnano.2014.149 (2014).

13 Zhu, H. *et al.* Lead halide perovskite nanowire lasers with low lasing thresholds and high quality factors. *Nature materials* **14**, 636-642 (2015).

14 Eaton, S. W. *et al.* Lasing in robust cesium lead halide perovskite nanowires. *Proceedings of the National Academy of Sciences* **113**, 1993-1998, doi:10.1073/pnas.1600789113 (2016).

15 Pourdavoud, N. *et al.* Photonic nanostructures patterned by thermal nanoimprint directly into organo‐metal halide perovskites. *Advanced Materials* **29**, 1605003 (2017).

16 Chen, S. & Nurmikko, A. Stable Green Perovskite Vertical-Cavity Surface-Emitting Lasers on Rigid and Flexible Substrates. *ACS Photonics* **4**, 2486-2494, doi:10.1021/acsphotonics.7b00713 (2017).

17 Wang, Y.-C. *et al.* Flexible organometal–halide perovskite lasers for speckle reduction in imaging projection. *ACS nano* **13**, 5421-5429 (2019).

18 Huang, C.-Y. *et al.* CsPbBr3 perovskite quantum dot vertical cavity lasers with low threshold and high stability. *Acs Photonics* **4**, 2281-2289 (2017).

19 Huang, C.-Y. *et al.* CsPbBr₃ Perovskite Quantum Dot Vertical Cavity Lasers with Low Threshold and High Stability. *ACS Photonics* **4**, 2281-2289, doi:10.1021/acsphotonics.7b00520 (2017).

20 Jia, Y., Kerner, R. A., Grede, A. J., Rand, B. P. & Giebink, N. C. Continuous-wave lasing in an organic–inorganic lead halide perovskite semiconductor. *Nature Photonics* **11**, 784-788, doi:10.1038/s41566-017-0047-6 (2017).

21 Zhu, H. *et al.* Lead halide perovskite nanowire lasers with low lasing thresholds and high quality factors. *Nature Materials* **14**, 636-642, doi:10.1038/nmat4271 (2015).

22 Zhang, H. *et al.* Room-temperature continuous-wave vertical-cavity surface-emitting lasers based on 2D layered organic–inorganic hybrid perovskites. *APL Materials* **9**, doi:10.1063/5.0052458 (2021).

23 Cegielski, P. J. *et al.* Monolithically Integrated Perovskite Semiconductor Lasers on Silicon Photonic Chips by Scalable Top-Down Fabrication. *Nano Letters* **18**, 6915-6923, doi:10.1021/acs.nanolett.8b02811 (2018).

24 Tao, S. *et al.* Absolute energy level positions in tin-and lead-based halide perovskites. *Nature communications* **10**, 1-10 (2019).

25 Wu, C. *et al.* Alternative type two-dimensional–three-dimensional lead halide perovskite with inorganic sodium ions as a spacer for high-performance light-emitting diodes. *ACS nano* **13**, 1645-1654 (2019).

26 Sim, K. *et al.* 18‐Crown‐6 Additive to Enhance Performance and Durability in Solution‐Processed Halide Perovskite Electronics. *Small* **18**, 2202298, doi:10.1002/smll.202202298 (2022).

27 Sutherland, B. R. *et al.* Perovskite thin films via atomic layer deposition. *Adv Mater* **27**, 53-58, doi:10.1002/adma.201403965 (2015).

28 Zhu, X. *et al.* Superior stability for perovskite solar cells with 20% efficiency using vacuum co-evaporation. *Nanoscale* **9**, 12316-12323, doi:10.1039/c7nr04501h (2017).

29 Han, D. *et al.* Efficient Light-Emitting Diodes Based on <i>in Situ</i> Fabricated FAPbBr₃ Nanocrystals: The Enhancing Role of the Ligand-Assisted Reprecipitation Process. *ACS Nano* **12**, 8808-8816, doi:10.1021/acsnano.8b05172 (2018).

30 Yakunin, S. *et al.* Low-threshold amplified spontaneous emission and lasing from colloidal nanocrystals of caesium lead halide perovskites. *Nature Communications* **6**, 8056, doi:10.1038/ncomms9056 (2015).

31 Zheng, X. *et al.* Chlorine Vacancy Passivation in Mixed Halide Perovskite Quantum Dots by Organic Pseudohalides Enables Efficient Rec. 2020 Blue Light-Emitting Diodes. *ACS Energy Lett.* **5**, 793-798, doi:10.1021/acsenergylett.0c00057 (2020).

32 Lin, J. *et al.* Perovskite Quantum Dots Glasses Based Backlit Displays. *ACS Energy Letters* **6**, 519-528, doi:10.1021/acsenergylett.0c02561 (2021).

33 Dai, S. W. *et al.* Perovskite Quantum Dots with Near Unity Solution and Neat-Film Photoluminescent Quantum Yield by Novel Spray Synthesis. *Adv Mater* **30**, doi:10.1002/adma.201705532 (2018).

34 Chen, Y. *et al.* 2D Ruddlesden-Popper Perovskites for Optoelectronics. *Advanced Materials* **30**, 1703487, doi:10.1002/adma.201703487 (2018).

35 Wang, N. *et al.* Perovskite light-emitting diodes based on solution-processed self-organized multiple quantum wells. *Nature Photonics* **10**, 699-704 (2016).

36 Wang, S., Cao, Y., Peng, Q., Huang, W. & Wang, J. Carrier Dynamics Determines the Optimization Strategies of Perovskite LEDs and PVs. *Research* **6**, doi:10.34133/research.0112 (2023).

37 Chen, J. *et al.* Carrier dynamic process in all-inorganic halide perovskites explored by photoluminescence spectra. *Photonics Research* **9**, 151, doi:10.1364/prj.410290 (2021).

38 Chen, Z. *et al.* Recombination Dynamics Study on Nanostructured Perovskite Light-Emitting Devices. *Advanced Materials* **30**, 1801370, doi:10.1002/adma.201801370 (2018).

39 Li, Y. *et al.* Exciton versus free carrier emission: Implications for photoluminescence efficiency and amplified spontaneous emission thresholds in quasi-2D and 3D perovskites. *Materials Today* **49**, 35-47, doi:10.1016/j.mattod.2021.05.002 (2021).

40 Xu, L. *et al.* Towards green antisolvent for efficient CH3NH3PbBr3 perovskite light emitting diodes: A comparison of toluene, chlorobenzene, and ethyl acetate. *Applied Physics Letters* **115**, 033101 (2019).

41 Song, J. *et al.* Room-Temperature Triple-Ligand Surface Engineering Synergistically Boosts Ink Stability, Recombination Dynamics, and Charge Injection toward EQE-11.6% Perovskite QLEDs. *Adv Mater* **30**, e1800764, doi:10.1002/adma.201800764 (2018).

42 Ban, M. *et al.* Solution-processed perovskite light emitting diodes with efficiency exceeding 15% through additive-controlled nanostructure tailoring. *Nature communications* **9**, 1-10 (2018).

43 Yuan, M. *et al.* Perovskite energy funnels for efficient light-emitting diodes. *Nature Nanotechnology* **11**, 872-877, doi:10.1038/nnano.2016.110 (2016).

44 Sun, Y. & Forrest, S. R. Enhanced light out-coupling of organic light-emitting devices using embedded low-index grids. *Nature Photonics* **2**, 483-487, doi:10.1038/nphoton.2008.132 (2008).

45 Richter, J. M. *et al.* Enhancing photoluminescence yields in lead halide perovskites by photon recycling and light out-coupling. *Nat Commun* **7**, 13941, doi:10.1038/ncomms13941 (2016).

46 Cho, C. *et al.* The role of photon recycling in perovskite light-emitting diodes. *Nat Commun* **11**, 611, doi:10.1038/s41467-020-14401-1 (2020).

47 Zou, C., Liu, Y., Ginger, D. S. & Lin, L. Y. Suppressing Efficiency Roll-Off at High Current Densities for Ultra-Bright Green Perovskite Light-Emitting Diodes. *ACS Nano* **14**, 6076-6086, doi:10.1021/acsnano.0c01817 (2020).

48 Sun, J., Li, F., Yuan, J. & Ma, W. Advances in Metal Halide Perovskite Film Preparation: The Role of Anti-Solvent Treatment. *Small Methods* **5**, 2100046 (2021).

49 Priante, D. *et al.* The recombination mechanisms leading to amplified spontaneous emission at the true-green wavelength in CH3NH3PbBr3 perovskites. *Applied Physics Letters* **106**, 081902 (2015).

50 Karnutsch, C. *et al.* Improved organic semiconductor lasers based on a mixed-order distributed feedback resonator design. *Applied Physics Letters* **90**, 131104 (2007).

51 Yan, D. *et al.* Ultrastable CsPbBr3 perovskite quantum dot and their enhanced amplified spontaneous emission by surface ligand modification. *Small* **15**, 1901173 (2019).

52 Tang, X. *et al.* Single halide perovskite/semiconductor core/shell quantum dots with ultrastability and nonblinking properties. *Advanced Science* **6**, 1900412 (2019).

53 Li, M. *et al.* Amplified spontaneous emission based on 2D Ruddlesden–Popper perovskites. *Advanced Functional Materials* **28**, 1707006 (2018).

54 Wang, L. *et al.* Ultralow-threshold and color-tunable continuous-wave lasing at room-temperature from in situ fabricated perovskite quantum dots. *The Journal of Physical Chemistry Letters* **10**, 3248-3253 (2019).

55 Chen, S., Zhang, C., Lee, J., Han, J. & Nurmikko, A. High-Q, low-threshold monolithic perovskite thin-film vertical-cavity lasers. *Advanced Materials* **29**, 1604781 (2017).

56 Wang, Y. *et al.* All-inorganic colloidal perovskite quantum dots: a new class of lasing materials with favorable characteristics. *Advanced materials* **27**, 7101-7108 (2015).

57 Gu, Z. *et al.* Direct-Writing Multifunctional Perovskite Single Crystal Arrays by Inkjet Printing. *Small* **13**, 1603217, doi:10.1002/smll.201603217 (2017).

58 Li, X. *et al.* Stable Whispering Gallery Mode Lasing from Solution-Processed Formamidinium Lead Bromide Perovskite Microdisks. *Advanced Optical Materials* **8**, 2000030, doi:10.1002/adom.202000030 (2020).

59 Pourdavoud, N. *et al.* Room-Temperature Stimulated Emission and Lasing in Recrystallized Cesium Lead Bromide Perovskite Thin Films. *Advanced Materials* **31**, 1903717, doi:10.1002/adma.201903717 (2019).

60 Cha, H., Bae, S., Jung, H., Ko, M. J. & Jeon, H. Single-Mode Distributed Feedback Laser Operation in Solution-Processed Halide Perovskite Alloy System. *Advanced Optical Materials* **5**, 1700545, doi:10.1002/adom.201700545 (2017).

61 Sandanayaka, A. S. *et al.* Indication of current-injection lasing from an organic semiconductor. *Applied Physics Express* **12**, 061010 (2019).

62 Qin, C. *et al.* Stable room-temperature continuous-wave lasing in quasi-2D perovskite films. *Nature* **585**, 53-57 (2020).

63 Zhao, L. *et al.* Nanosecond-Pulsed Perovskite Light-Emitting Diodes at High Current Density. *Adv Mater* **33**, e2104867, doi:10.1002/adma.202104867 (2021).

64 Moon, J. *et al.* Quasi-CW Lasing from Directly Patterned and Encapsulated Perovskite Cavity at 260 K. *ACS Photonics* **9**, 1984-1991, doi:10.1021/acsphotonics.2c00071 (2022).

65 Chang, C., Shi, Y., Zou, C. & Lin, L. Y. MAPbBr ₃ First-Order Distributed Feedback Laser with High Stability. *Advanced Photonics Research*, 2200071, doi:10.1002/adpr.202200071 (2022).

66 Henry, C. Theory of the linewidth of semiconductor lasers. *IEEE Journal of Quantum Electronics* **18**, 259-264, doi:10.1109/jqe.1982.1071522 (1982).

67 De Giorgi, M. L., Krieg, F., Kovalenko, M. V. & Anni, M. Amplified Spontaneous Emission Threshold Reduction and Operational Stability Improvement in CsPbBr3 Nanocrystals Films by Hydrophobic Functionalization of the Substrate. *Scientific Reports* **9**, doi:10.1038/s41598-019-54412-7 (2019).

68 Rehman, W. *et al.* Charge-Carrier Dynamics and Mobilities in Formamidinium Lead Mixed-Halide Perovskites. *Advanced Materials* **27**, 7938-7944, doi:10.1002/adma.201502969 (2015).

69 Yang, Y. *et al.* Comparison of Recombination Dynamics in CH₃NH₃PbBr₃ and CH₃NH₃PbI₃ Perovskite Films: Influence of

Exciton Binding Energy. *The Journal of Physical Chemistry Letters* **6**, 4688-4692, doi:10.1021/acs.jpclett.5b02290 (2015).

70 Kim, T.-H. *et al.* Full-colour quantum dot displays fabricated by transfer printing. *Nature Photonics* **5**, 176-182, doi:10.1038/nphoton.2011.12 (2011).

71 Dai, X., Deng, Y., Peng, X. & Jin, Y. Quantum-Dot Light-Emitting Diodes for Large-Area Displays: Towards the Dawn of Commercialization. *Adv Mater* **29**, doi:10.1002/adma.201607022 (2017).

72 Wu, W. *et al.* Flexible Photodetector Arrays Based on Patterned CH3 NH3 PbI3- x Clx Perovskite Film for Real-Time Photosensing and Imaging. *Adv Mater* **31**, e1805913, doi:10.1002/adma.201805913 (2019).

73 Prins, F. *et al.* Direct Patterning of Colloidal Quantum-Dot Thin Films for Enhanced and Spectrally Selective Out-Coupling of Emission. *Nano Lett* **17**, 1319-1325, doi:10.1021/acs.nanolett.6b03212 (2017).

74 Lee, E. K. *et al.* Chemically Robust Ambipolar Organic Transistor Array Directly Patterned by Photolithography. *Adv Mater* **29**, doi:10.1002/adma.201605282 (2017).

75 Park, J.-S. *et al.* Alternative patterning process for realization of large-area, full-color, active quantum dot display. *Nano letters* **16**, 6946-6953 (2016).

76 Ji, T., Jin, S., Zhang, H., Chen, S. & Sun, X. W. Full color quantum dot light-emitting diodes patterned by photolithography technology. *Journal of the Society for Information Display* **26**, 121-127, doi:10.1002/jsid.640 (2018).

77 Lin, S. *et al.* Multi-primary-color quantum-dot down-converting films for display applications. *Opt Express* **27**, 28480-28493, doi:10.1364/OE.27.028480 (2019).

78 Lyashenko, D., Perez, A. & Zakhidov, A. High-resolution patterning of organohalide lead perovskite pixels for photodetectors using orthogonal photolithography. *physica status solidi (a)* **214**, doi:10.1002/pssa.201600302 (2017).

79 Yang, X., Wu, J., Liu, T. & Zhu, R. Patterned Perovskites for Optoelectronic Applications. *Small Methods* **2**, doi:10.1002/smtd.201800110 (2018).

80 Zou, C., Chang, C., Sun, D., Bohringer, K. F. & Lin, L. Y. Photolithographic Patterning of Perovskite Thin Films for Multicolor Display Applications. *Nano Lett* **20**, 3710-3717, doi:10.1021/acs.nanolett.0c00701 (2020).